Prandtl number dependence in turbulent compressible convection

Lekha Sharma,* Mayank Pathak,† and Harshit Tiwari‡
Department of Physics, Indian Institute of Technology Kanpur, Kanpur 208016, India

Mahendra K. Verma§
Department of Physics, Indian Institute of Technology Kanpur, Kanpur 208016, India
and Kotak School of Sustainability, Indian Institute of Technology Kanpur, Kanpur 208016, India

(Received 6 July 2025; accepted 16 October 2025; published 19 November 2025)

In this work, we report a comprehensive study of turbulent compressible convection through two-dimensional (2D) and three-dimensional (3D) numerical simulations spanning a wide range of Prandtl numbers ($10^{-2} \leqslant \mathrm{Pr} \leqslant 10^{2}$) and Rayleigh numbers ($\mathrm{Ra} = 10^{7}, 10^{8}, 10^{9}$). The total temperature exhibits adiabatic cooling in the bulk, with minimal variation across Pr. For $\mathrm{Pr} < 1$ and > 1, the Nusselt number scales as $\mathrm{Ra}^{0.22}\mathrm{Pr}^{0.04}$ and $\mathrm{Ra}^{0.28}\mathrm{Pr}^{0.02}$ in 2D, and as $\mathrm{Ra}^{0.27}\mathrm{Pr}^{0.16}$ and $\mathrm{Ra}^{0.27}\mathrm{Pr}^{0.03}$ in 3D. The corresponding variations for the Reynolds number are $\mathrm{Ra}^{0.51}\mathrm{Pr}^{-0.78}$ and $\mathrm{Ra}^{0.60}\mathrm{Pr}^{-0.99}$ in 2D, and $\mathrm{Ra}^{0.45}\mathrm{Pr}^{-0.64}$ and $\mathrm{Ra}^{0.51}\mathrm{Pr}^{-0.91}$ in 3D. Top-bottom asymmetry persists in both the thermal and viscous boundary layers, with thicker top layers. As Pr increases, thermal boundary layers become thinner while viscous boundary layers thicken, with distinct scaling near the top and bottom boundaries.

DOI: 10.1103/vkvv-l3m4

I. INTRODUCTION

Turbulent convection is observed in a wide range of natural and industrial systems, including stellar interiors, planetary atmospheres, and engineering applications [1–5]. A key parameter influencing the behavior of such flows is the Prandtl number (Pr), defined as the ratio of momentum diffusivity to thermal diffusivity. It characterizes the relative importance of viscous and thermal effects in convective processes. Low Prandtl number fluids, where thermal diffusion dominates, are commonly found in stellar interiors like the solar convection zone, with $\mathrm{Pr} \approx 10^{-4}$–$10^{-6}$, plantery cores like the Earth's liquid outer core, with $\mathrm{Pr} \sim 10^{-2}$, and liquid metals [2,5–7]. The Earth's atmosphere has Pr near unity. High-Pr fluids, where viscous forces prevail, appear in substances like oils and molten polymers, and in the Earth's mantle [6,8,9]. Understanding the effects of Pr across these diverse regimes is essential for characterizing the intricate dynamics of turbulent convection.

A common approach to studying convection is the Rayleigh-Bénard convection (RBC), where a fluid layer confined between two horizontal plates is heated from below and cooled from the top [1–4,10]. It often employs the Boussinesq approximation, assuming constant fluid properties and accounting for temperature effects only in the buoyancy term. However, convective regions in planets and stars typically exhibit significant density stratification [5,11–13], making the Boussinesq assumption unsuitable. To study such systems, a fully compressible framework is essential,

*Contact author: lekhas@iitk.ac.in
†Contact author: mpathak@iitk.ac.in
‡Contact author: tharshit@iitk.ac.in
§Contact author: mkv@iitk.ac.in

as it captures variations in density, pressure, and temperature that significantly influence the convective dynamics [12–16]. Compressible convection exhibits additional complexities due to density stratification and the presence of an adiabatic background state. Despite its relevance to astrophysical and geophysical flows, the influence of Pr on compressible convection remains largely unexplored.

The effect of Pr on RBC has been extensively studied in numerous experiments and numerical simulations [17–23]. These studies have established that Pr plays a pivotal role in governing the structure and dynamics of thermal convection. High-Pr convection tends to be more laminar and organized, often characterized by plume-dominated regimes [8,22,24–26]. In contrast, low-Pr convection, where inertia is more significant, the flow becomes highly turbulent, leading to the formation of coherent large-scale circulations [8,22,26–28]. Several studies on RBC have also explored turbulent convection at extreme Rayleigh numbers (Ra) [17,29–33]. It has been observed that RBC exhibits diverse flow morphologies depending on both Ra and Pr. Extensive work on RBC has focused on the scaling of global quantities like the Nusselt number (Nu) and Reynolds number (Re) with Ra and Pr [2,33–38]. These are often expressed as power laws of the form $\mathrm{Nu} \sim \mathrm{Ra}^{\alpha}\mathrm{Pr}^{\beta}$ and $\mathrm{Re} \sim \mathrm{Ra}^{\delta}\mathrm{Pr}^{\gamma}$. For Nu, the exponents α and β range from 1/4 to 1/3 and 0.14 to approximately 0, respectively, as Pr increases from $\ll 1$ to $\gtrsim 1$ [8,18,21,39,40]; for Re, δ and γ vary from 0.4 to 0.6 and -0.7 to -0.95, respectively, as Pr increases from $\ll 1$ to $\gg 1$ [18,19,26,34,41,42]. Grossmann and Lohse [34] developed a unified theory to explain these trends based on the relative contributions of bulk and boundary layer dissipation, which has since been refined and extended to higher Ra and Pr [18,26,35,38,43].

In contrast, the role of Pr in compressible convection remains far less explored. While the infinite-Pr limit has been studied in various contexts, these works are limited to linear analysis, with nonlinear solutions considered only at moderate Rayleigh numbers [9,13,44–46]. For low-Pr fluids, Toomre *et al.* [47] conducted early three-dimensional simulations of compressible convection in stratified atmospheres, highlighting asymmetries and plume-dominated flows. Singh and Chan [48] considered a wide range of low-Pr fluids to explore compressible convection in deep stellar atmospheres, emphasizing its influence on convective structure and dynamics. Käpylä *et al.* [49] systematically examined the Pr dependence in stellar convection, focusing on flow statistics and convective energy transport. In the high-Pr regime, Manga and Weeraratne [50] reported plume-dominated convection and absence of large-scale circulation, similar to RBC. Anders and Brown [51] and Verhoeven *et al.* [16] studied the effect of Ra and superadiabaticity on Nu at fixed Pr. John and Schumacher [52] explored the different regimes of fully compressible convection at $\mathrm{Pr} = 0.7$. However, these studies have focused on low or moderate Ra. For very large Ra, Tiwari *et al.* [53] investigated Nu and Re scalings up to $\mathrm{Ra} = 10^{15}$ in two-dimensions (2D) and $= 10^{11}$ in three-dimensions (3D), but with Pr fixed at 0.7. Consequently, the combined influence of Ra and Pr on these global scalings remains unclear.

In this work, we address this gap by performing extensive numerical simulations of turbulent compressible convection across a broad range of Ra (10^7, 10^8, 10^9) and Pr ($0.01 \leqslant \mathrm{Pr} \leqslant 100$). We solve the fully compressible equations in both 2D and 3D using our in-house finite-difference Python solver *Dhara* [53], that employs the MacCormack-total variation diminishing (MacCormack-TVD) scheme [54–56]. Our analysis focuses on the influence of Pr on flow organization in the bulk and near the boundaries, temperature and velocity field profiles, the scaling behavior of Nu and Re, and the structure and scaling of thermal and viscous boundary layers. We also contrast our findings with those known for RBC to highlight similarities and differences arising from compressibility effects.

The structure of the paper is as follows. In Sec. II, we describe the physical system, governing equations, and discuss some past results. Section III outlines the numerical methods and simulation details. In Sec. IV, we present the flow morphology, energetics, and vertical field profiles. The scaling of global quantities is discussed in Sec. V, followed by an analysis of boundary layer properties in Sec. VI. Finally, some conclusive remarks are provided in Sec. VII.

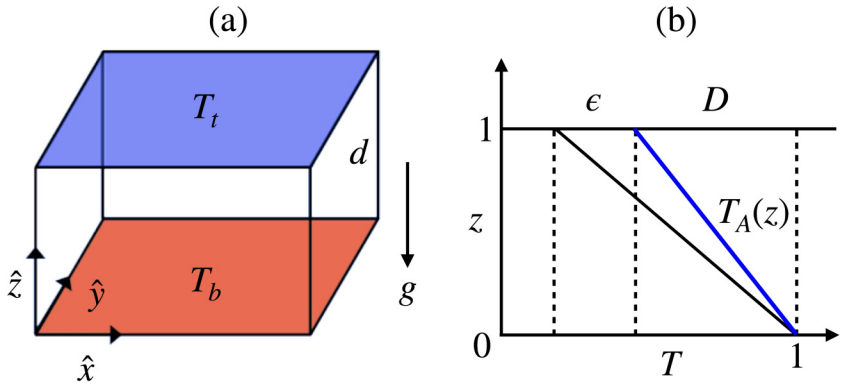

FIG. 1. (a) Schematic diagram of the physical system with height d. The bottom and top plates are maintained at temperatures T_b and T_t, respectively, with gravity g acting in the downward direction. (b) Nondimensional adiabatic temperature profile $T_A(z)$ (blue line) and the total temperature profile (black line), adapted from Tiwari *et al.* [53].

II. GOVERNING EQUATIONS AND PAST WORKS ON Pr DEPENDENCE

A fully compressible fluid confined within a rectangular domain of dimensions $L \times L \times d$ in 3D and $L \times d$ in 2D, with L and d as the length and height of the box, is considered for the present study. The fluid is subjected to a vertical temperature gradient $\Delta = (T_b - T_t)/d > 0$, with the bottom wall maintained at a higher temperature T_b and the top wall at a lower temperature T_t. A schematic illustration of the physical system is presented in Fig. 1(a). The nondimensional governing equations for the convective motion of the compressible fluid in conservative form are given by [12,14,52]

$$\frac{\partial \rho}{\partial t} + \frac{\partial}{\partial x_i}(\rho u_i) = 0, \tag{1}$$

$$\frac{\partial}{\partial t}(\rho u_i) + \frac{\partial}{\partial x_j}(\rho u_i u_j + \delta_{ij} p - \tau_{ij}) = -\frac{1}{\epsilon}\rho \delta_{iz}, \tag{2}$$

$$\frac{\partial E}{\partial t} + \frac{\partial}{\partial x_i}\left(u_i(E+p) - \frac{1}{\epsilon D\sqrt{\mathrm{Ra}Pr}}\frac{\partial T}{\partial x_i} - u_j \tau_{ij}\right) = 0, \tag{3}$$

along with an ideal gas equation of state. Here, ρ, $\mathbf{u} = (u_1, u_2, u_3)$, T, p, E, and τ_{ij} are the nondimensionalized density, velocity, temperature, pressure, total energy, and stress-tensor, respectively. Equations (1)–(3) are nondimensionalized with d as the characteristic length, the free-fall velocity $\sqrt{\epsilon g d}$ as the velocity scale, and reference density ρ_b and temperature T_b as the density and temperature scales. The system is governed by four key dimensionless parameters, which are [16,52]

$$\text{Rayleigh number Ra} = \frac{\epsilon g d^3}{\nu \kappa}, \tag{4}$$

$$\text{Prandtl number Pr} = \frac{\nu}{\kappa}, \tag{5}$$

$$\text{superadiabaticity } \epsilon = \frac{d}{T_b}\left(\frac{\Delta}{d} - \frac{g}{C_p}\right), \tag{6}$$

$$\text{dissipation number } D = \frac{gd}{T_b C_p}. \tag{7}$$

Another important parameter is the aspect ratio of the box, $\Gamma = L/d$. Here, ν and κ are the fluid's kinematic viscosity and thermal diffusivity, g is the gravitational acceleration that acts in

the negative z direction, and C_p is the specific heat capacity at constant pressure. The fluid is assumed to have constant dynamic viscosity $\mu = \nu\rho$ and thermal conductivity $K = \kappa C_p \rho$. In the absence of convection, the compressible fluid maintains a hydrostatic adiabatic equilibrium where the temperature, density, and pressure profiles are [16]

$$T_A(z) = (1 - Dz), \tag{8}$$

$$\rho_A(z) = (1 - Dz)^{\beta}, \tag{9}$$

$$p_A(z) = (1 - Dz)^{(\beta+1)}, \tag{10}$$

where $\beta = 1/(\gamma - 1)$ is the adiabatic index, with $\gamma = C_p/C_V$ and C_V is the specific heat capacity at constant volume. This stratified equilibrium serves as a reference state for the analysis of convective deviations. The superadiabatic temperature $T_{\rm sa}$, which quantifies the deviation from the adiabatic temperature profile and acts as the driving force for convection, is defined as

$$T_{\rm sa}(\mathbf{r}, t) = T(\mathbf{r}, t) - T_A(z). \tag{11}$$

Figure 1(b) illustrates both the adiabatic background profile and the total temperature field for reference.

We consider no-slip boundary conditions for the velocity field and perfectly conducting boundaries for the temperature field on both the top and bottom plates. Along the sidewalls, periodic boundary conditions are applied.

The global response parameters of the system are the Nusselt number (Nu) and the Reynolds number (Re), which measure the large-scale heat and momentum transport in turbulent convection, respectively. The Nusselt number, Nu, can be defined in several ways, with the most commonly used being the *bulk* (or volume) Nusselt number and the *boundary* Nusselt number. The *bulk* Nu is defined as the ratio of excess total heat flux over the adiabatic heat flux to the excess conductive heat flux over the adiabatic value and is given by [14,53]

$$\mathrm{Nu} = 1 + \frac{\sqrt{\mathrm{RaPr}}}{\epsilon}\langle \rho u_z T_{\rm sa}\rangle_{V,t} + \frac{D\sqrt{\mathrm{RaPr}}}{2}\langle \rho u_z u^2\rangle_{V,t} = 1 + \mathrm{Nu}_{\rm conv} + \mathrm{Nu}_K, \tag{12}$$

where $\mathrm{Nu}_{\rm conv}$ and Nu_K represent the convective and kinetic contributions to the Nusselt number, respectively. Here, $\langle\cdot\rangle_{V,t}$ denotes the combined volume-time average. The *boundary* Nu is calculated using the heat flux at the top and bottom boundaries and is expressed as [16,53,57]

$$\mathrm{Nu} = -\frac{1}{2\epsilon}\left[\left.\frac{d\langle T_{\rm sa}\rangle_{A,t}}{dz}\right|_{z=0} + \left.\frac{d\langle T_{\rm sa}\rangle_{A,t}}{dz}\right|_{z=1}\right], \tag{13}$$

where $\langle . \rangle_{A,t}$ represents the planar and temporal average. We verified that Nu computed from both definitions yields nearly identical values. However, the values obtained using the *bulk* Nu [Eq. (12)] show larger fluctuations compared to those from the *boundary* Nu [Eq. (13)], especially for 2D flows [58]. Therefore, in this paper, we report Nu values based on the *boundary* Nu [Eq. (13)]. The Reynolds number, Re, is defined as [10,16]

$$\mathrm{Re} = \frac{\tilde{U} d}{\nu} = \sqrt{\frac{\mathrm{Ra}}{\mathrm{Pr}}}U, \tag{14}$$

where $\tilde{U}$ is the dimensional rms velocity, and U is its nondimensional counterpart.

Extensive literature exists on the scaling of Nu and Re with Ra and Pr for turbulent RBC. In one of the earliest theoretical models, Malkus [59] proposed that heat transport in turbulent convection is limited by the most unstable modes of the boundary layers, predicting $\mathrm{Nu} \sim \mathrm{Ra}^{1/3}$ scaling. Kraichnan [60] advanced the theory for extremely large Ra and deduced that $\mathrm{Nu} \sim \mathrm{Ra}^{1/2}\mathrm{Pr}^{1/2}$, $\mathrm{Re} \sim \mathrm{Ra}^{1/2}\mathrm{Pr}^{-1/2}$ for Pr <0.1, whereas for $0.1 < \mathrm{Pr} \leqslant 1$, the scalings become $\mathrm{Nu} \sim \mathrm{Ra}^{1/2}\mathrm{Pr}^{-1/4}$, $\mathrm{Re} \sim \mathrm{Ra}^{1/2}\mathrm{Pr}^{-3/4}$, with possible logarithmic corrections. Later, Castaing *et al.* [24] conducted experiments using helium gas and found $\mathrm{Nu} \sim \mathrm{Ra}^{2/7}$ and $\mathrm{Re} \sim \mathrm{Ra}^{3/7}$. Simultaneously, Shraiman

and Siggia [61] presented scaling arguments incorporating both bulk and boundary layer contributions, leading to $\mathrm{Nu} \sim \mathrm{Ra}^{2/7}\mathrm{Pr}^{-1/7}$, $\mathrm{Re} \sim \mathrm{Ra}^{3/7}\mathrm{Pr}^{-5/7}$. Verzicco and Camussi [8] conducted both experiments and high-resolution direct numerical simulations (DNS) for a wide range of Pr and reported $\mathrm{Nu} \sim \mathrm{Pr}^{0.14}$ for low-Pr, with Nu becoming nearly Pr-independent at high-Pr. With Ra, they found $\mathrm{Nu} \sim \mathrm{Ra}^{0.25}$ for low-Pr and $\mathrm{Nu} \sim \mathrm{Ra}^{0.285}$ for high-Pr. Additionally, $\mathrm{Re} \sim \mathrm{Pr}^{-0.73}$ for low-Pr and $\mathrm{Re} \sim \mathrm{Pr}^{-0.94}$ for high-Pr; $\mathrm{Re} \sim \mathrm{Ra}^{0.53}$ for both low- and high-Pr. A unified scaling theory that combined boundary layer and bulk dissipation contributions, producing a detailed phase diagram of scaling regimes for Nu and Re as functions of Ra and Pr was provided by Grossmann and Lohse [34] (GL theory).

GL theory was later refined and compared extensively with experimental and numerical data in subsequent works [22,35,62]. For very large Pr, Grossmann and Lohse [35] predicted $\mathrm{Nu} \sim \mathrm{Ra}^{1/3}\mathrm{Pr}^{0}$ and $\mathrm{Re} \sim \mathrm{Ra}^{2/3}\mathrm{Pr}^{-1}$–a regime further explored by Bhattacharya *et al.* [38]. The Pr-independence of Nu and linear inverse scaling of Re with Pr in the high-Pr regime were subsequently confirmed by experiments and numerical simulations [18,26,37,43]. Lam *et al.* [19] reported that for Pr ranging from 6 to 1027, the scaling exponents of Re (based on the maximum velocity of circulating wind) varied from 0.5 to 0.68 for Ra and −0.88 to −0.95 for Pr. Breuer *et al.* [22] conducted 3D DNS for $10^{-3} \leqslant \mathrm{Pr} \leqslant 10^{2}$ at a fixed $\mathrm{Ra} = 10^{6}$, and obtained $\mathrm{Nu} \sim \mathrm{Pr}^{0.182}$ for $\mathrm{Pr} \ll 1$ and $\sim \mathrm{Pr}^{0.032}$ for $\mathrm{Pr} > 0.3$. Their data also yields $\mathrm{Re} \sim \mathrm{Pr}^{-0.607}$ for low-Pr and $\mathrm{Re} \sim \mathrm{Pr}^{-0.998}$ for high-Pr. Comparisons with 2D results [63,64] revealed that Nu and Re scaling behaviors diverge significantly from 3D for $\mathrm{Pr} < 1$, but are similar for high Pr. Silano *et al.* [26] carried out comprehensive DNS for a wide range of Ra ($10^{5} \leqslant \mathrm{Ra} \leqslant 10^{9}$) and Pr ($10^{-1} \leqslant \mathrm{Pr} \leqslant 10^{4}$) and observed that Nu scales as $\mathrm{Ra}^{2/7}$ for $\mathrm{Pr} = 1$ and as $\mathrm{Ra}^{0.31}$ for $\mathrm{Pr} = 10^{3}$; while Re follows $\mathrm{Ra}^{1/2}\mathrm{Pr}^{-1}$, ignoring logarithmic corrections. Similarly, Stevens *et al.* [65] reported $\mathrm{Nu} \sim \mathrm{Ra}^{1/3}$ using 3D DNS. Scheel and Schumacher [27] found $\mathrm{Nu} \sim \mathrm{Ra}^{0.26}$ for $\mathrm{Pr} \ll 1$. Recent quasi-2D experiments by Li *et al.* [66] reported $\mathrm{Re} \sim \mathrm{Ra}^{0.58}\mathrm{Pr}^{-0.82}$ and $\mathrm{Nu} \sim \mathrm{Ra}^{0.289}\mathrm{Pr}^{-0.02}$ in the high-Pr regime. In low-Pr 2D simulations, Zhang and Zhou [28] found $\mathrm{Nu} \sim \mathrm{Pr}^{0.14}$, $\mathrm{Re} \sim \mathrm{Pr}^{-0.82}$ at $\mathrm{Ra} = 10^{7}$ and $\mathrm{Nu} \sim \mathrm{Pr}^{0.11}$, $\mathrm{Re} \sim \mathrm{Pr}^{-0.93}$ at $\mathrm{Ra} = 10^{8}$.

In contrast, very few studies have examined the scalings of Nu and Re in compressible convection, especially with respect to both Ra and Pr. Among those, Manga and Weeraratne [50] conducted experiments at low Ra ($< 10^{5}$) and large Pr ($10^{3} < \mathrm{Pr} < 10^{6}$) and found $\mathrm{Nu} \sim \mathrm{Ra}^{0.281}$. Anders and Brown [51] performed 2D and 3D simulations at $\mathrm{Pr} = 1$ and observed $\mathrm{Nu} \sim \mathrm{Ra}^{1/3}$ for low to moderate Ra ($\mathrm{Ra} < 10^{4}$), transitioning to $\mathrm{Ra}^{1/5}$ for $\mathrm{Ra} > 10^{4}$ in 2D; whereas in 3D, $\mathrm{Nu} \sim \mathrm{Ra}^{2/7}$, similar to RBC. Re scales as $\sim \mathrm{Ra}^{3/4}$ at low Ra in 2D; as $\sim \mathrm{Ra}^{1/2}$ in 3D and for high Ra in 2D [51]. Recently, Tiwari *et al.* [53] reported $\mathrm{Nu} \sim \mathrm{Ra}^{1/3}$ and $\mathrm{Re} \sim \mathrm{Ra}^{1/2}$ in both 2D and 3D for high Ra at $\mathrm{Pr} = 0.7$.

From the above, it is evident that the combined effect of Ra and Pr on compressible convection—particularly on the scaling of Nu and Re—remains largely unexplored. This knowledge gap forms the primary motivation of the present work, which aims to advance the understanding of scaling laws in compressible turbulent convection.

In the next section, we detail the numerical simulations, followed by an in-depth discussion of the results.

III. SIMULATION DETAILS

We numerically solve Eqs. (1)–(3) on a collocated grid using the finite-difference code—*Dhara* [53]—which implements the computationally efficient MacCormack-TVD scheme [54–56,67]. The governing equations are first written in conservative form as

$$\frac{\partial Q}{\partial t} + \frac{\partial F_i}{\partial x_i} = S_i, \tag{15}$$

where Q, F_i, and S_i contain field variables, fluxes, and source terms, respectively. This equation is then decomposed into one-dimensional equations using the operator-splitting method, which are then advanced in time using the MacCormack scheme. Finally, we apply the TVD approach which

TABLE I. Details of the numerical simulations for 2D convection: the Prandtl number (Pr), the Rayleigh number (Ra), the grid size, the Reynolds number (Re), the Nusselt number (Nu), the thermal boundary layer thicknesses near the top and bottom boundaries (λ_T^t and λ_T^b, respectively), and the viscous boundary layer thicknesses near the top and bottom boundaries (λ_V^t and λ_V^b, respectively). The other parameters are aspect ratio $\Gamma = 1$, superadiabaticity $\epsilon = 0.1$, dissipation number $D = 0.5$, and ratio of specific heats $\gamma = 1.3$.

Pr	Ra	Grid size	Re	Nu	λ_T^t	λ_T^b	λ_V^t	λ_V^b
0.01	10^7	1501^2	$(2.93 \pm 0.05) \times 10^4$	8.89 ± 0.29	0.2287	0.0533	0.0550	0.0190
0.01	10^8	2049^2	$(8.15 \pm 0.38) \times 10^4$	11.33 ± 2.07	0.1519	0.0405	0.0405	0.0172
0.01	10^9	3001^2	$(2.19 \pm 0.04) \times 10^5$	16.58 ± 1.36	0.1324	0.0273	0.0248	0.0136
0.05	10^7	1201^2	$(9.22 \pm 0.14) \times 10^3$	8.42 ± 0.22	0.1883	0.0367	0.0624	0.0208
0.05	10^8	1501^2	$(2.91 \pm 0.12) \times 10^4$	11.60 ± 1.47	0.1407	0.0313	0.0420	0.0234
0.05	10^9	2001^2	$(7.84 \pm 0.26) \times 10^4$	17.98 ± 2.08	0.1044	0.0256	0.0256	0.0160
0.1	10^7	513^2	$(5.10 \pm 0.15) \times 10^3$	7.74 ± 0.40	0.1934	0.0332	0.0664	0.0232
0.1	10^8	513^2	$(1.70 \pm 0.50) \times 10^4$	11.83 ± 1.24	0.1348	0.0293	0.0449	0.0156
0.1	10^9	1001^2	$(5.06 \pm 0.19) \times 10^4$	19.69 ± 0.75	0.0980	0.0248	0.0273	0.0144
0.5	10^7	513^2	$(1.141 \pm 0.004) \times 10^3$	6.47 ± 0.07	0.1699	0.0312	0.0845	0.0280
0.5	10^8	513^2	$(3.76 \pm 0.02) \times 10^3$	12.27 ± 0.21	0.1152	0.0234	0.0547	0.0165
0.5	10^9	701^2	$(1.63 \pm 0.06) \times 10^4$	22.27 ± 1.48	0.0836	0.0199	0.0312	0.0150
0.7	10^7	257^2	$(8.224 \pm 0.001) \times 10^2$	6.963 ± 0.002	0.1602	0.0273	0.0938	0.0285
0.7	10^8	257^2	$(2.95 \pm 0.09) \times 10^3$	12.1 ± 0.3	0.1094	0.0215	0.0642	0.0215
0.7	10^9	513^2	$(1.20 \pm 0.05) \times 10^4$	21.07 ± 1.02	0.0797	0.0176	0.0376	0.0232
5	10^7	257^2	$(1.65 \pm 0.21) \times 10^2$	7.34 ± 0.67	0.1523	0.0508	0.1250	0.0820
5	10^8	257^2	$(6.53 \pm 0.52) \times 10^2$	13.59 ± 1.06	0.0898	0.0312	0.0898	0.0580
5	10^9	513^2	$(2.71 \pm 0.11) \times 10^3$	28.97 ± 0.91	0.0547	0.0215	0.0582	0.0328
25	10^7	257^2	$(3.24 \pm 0.55) \times 10^1$	7.65 ± 0.50	0.1406	0.0469	0.1699	0.0859
25	10^8	257^2	$(1.31 \pm 0.16) \times 10^2$	14.52 ± 0.74	0.0859	0.0312	0.1172	0.1055
25	10^9	513^2	$(5.54 \pm 0.45) \times 10^2$	27.49 ± 1.50	0.0508	0.0195	0.1095	0.0857
50	10^7	257^2	$(1.68 \pm 0.29) \times 10^1$	7.88 ± 0.36	0.1289	0.0469	0.1352	0.0829
50	10^8	257^2	$(6.42 \pm 0.79) \times 10^1$	14.55 ± 0.79	0.0859	0.0273	0.1445	0.0938
50	10^9	513^2	$(2.70 \pm 0.24) \times 10^2$	27.70 ± 0.84	0.0488	0.0195	0.1124	0.0965
75	10^7	257^2	$(1.15 \pm 0.19) \times 10^1$	7.90 ± 0.47	0.1250	0.0436	0.1588	0.0625
75	10^8	257^2	$(4.13 \pm 0.61) \times 10^1$	14.67 ± 0.88	0.0820	0.0273	0.1445	0.0859
75	10^9	513^2	$(1.72 \pm 0.15) \times 10^2$	28.94 ± 1.04	0.0469	0.0176	0.1324	0.1289
100	10^7	257^2	9.22 ± 0.86	8.04 ± 0.10	0.1172	0.0436	0.1406	0.0781
100	10^8	257^2	$(3.27 \pm 0.67) \times 10^1$	14.82 ± 0.86	0.0781	0.0234	0.1588	0.0977
100	10^9	513^2	$(1.39 \pm 0.10) \times 10^2$	28.69 ± 0.69	0.0449	0.0156	0.1324	0.1289

introduces a flux limiter function to ensure that the solution remains free of spurious oscillations and also preserves monotonicity [54,56]. This method is second-order accurate in both space and time. Our results are insensitive to the choice of numerical scheme, as demonstrated in the Appendix.

For boundary conditions, second-order forward differences are applied at the bottom plate and second-order backward differences at the top. No-slip and perfectly conducting boundary conditions are imposed at the top and bottom plates, whereas periodic boundary conditions are imposed on the sidewalls. To better resolve steep gradients near the thermal and viscous boundary layers, we employ either a uniform grid or a nonuniform tangent-hyperbolic grid in the z-direction depending on the parameters. Uniform spacing is used in the horizontal directions.

We perform a total of 60 numerical simulations, with 30 cases each in 2D and 3D. All simulations use fixed parameters: $\Gamma = 1$, $\gamma = 1.3$, $\epsilon = 0.1$, and $D = 0.5$. We explore ten values of the Prandtl number, Pr $= 0.01,\ 0.05,\ 0.1,\ 0.5,\ 0.7,\ 5,\ 25,\ 50,\ 75,\ 100$ and three Rayleigh numbers, Ra $= 10^7$, 10^8, and 10^9. Depending on the values of Ra and Pr, the grid resolution ranges from 257^2 to 3001^2 in 2D and from 257^3 to 701^3 in 3D. Refer to Tables I and II for the simulation details. In the tables, we report Pr, Ra, grid sizes, the Reynolds number (Re), the boundary Nusselt number

TABLE II. Details of the numerical simulations for 3D convection: the Prandtl number (Pr), the Rayleigh number (Ra), the grid size, the Reynolds number (Re), the Nusselt number (Nu), the thermal boundary layer thicknesses near the top and bottom boundaries (λ_T^t and λ_T^b, respectively), and the viscous boundary layer thicknesses near the top and bottom boundaries (λ_V^t and λ_V^b, respectively). The other parameters are aspect ratio $\Gamma = 1$, superadiabaticity $\epsilon = 0.1$, dissipation number $D = 0.5$, and ratio of specific heats $\gamma = 1.3$.

Pr	Ra	Grid size	Re	Nu	λ_T^t	λ_T^b	λ_V^t	λ_V^b
0.01	10^7	401^3	$(1.13 \pm 0.03) \times 10^4$	3.92 ± 0.23	0.2525	0.0375	0.0550	0.0150
0.01	10^8	401^3	$(3.13 \pm 0.05) \times 10^4$	7.26 ± 0.14	0.1775	0.0350	0.0375	0.0125
0.01	10^9	701^3	$(8.79 \pm 0.16) \times 10^4$	13.97 ± 0.52	0.1166	0.0279	0.0243	0.0071
0.05	10^7	401^3	$(4.36 \pm 0.07) \times 10^3$	5.55 ± 0.25	0.2050	0.0350	0.0635	0.0175
0.05	10^8	401^3	$(1.21 \pm 0.02) \times 10^4$	10.17 ± 0.10	0.1375	0.0325	0.0401	0.0150
0.05	10^9	701^3	$(3.30 \pm 0.07) \times 10^4$	19.46 ± 0.44	0.0915	0.0261	0.0243	0.0114
0.1	10^7	257^3	$(2.76 \pm 0.06) \times 10^3$	6.32 ± 0.29	0.1836	0.0312	0.0702	0.0201
0.1	10^8	257^3	$(7.71 \pm 0.24) \times 10^3$	11.30 ± 0.43	0.1250	0.0312	0.0410	0.0185
0.1	10^9	701^3	$(2.14 \pm 0.11) \times 10^4$	21.83 ± 0.79	0.0812	0.0243	0.0279	0.0128
0.5	10^7	257^3	$(9.04 \pm 0.42) \times 10^2$	7.96 ± 0.44	0.1523	0.0273	0.0859	0.0234
0.5	10^8	257^3	$(2.65 \pm 0.08) \times 10^3$	14.04 ± 0.41	0.1055	0.0273	0.0508	0.0217
0.5	10^9	701^3	$(7.62 \pm 0.11) \times 10^3$	26.66 ± 0.83	0.0689	0.0205	0.0334	0.0157
0.7	10^7	257^3	$(7.10 \pm 0.43) \times 10^2$	7.93 ± 0.44	0.1328	0.0273	0.0859	0.0234
0.7	10^8	257^3	$(2.11 \pm 0.09) \times 10^3$	14.45 ± 0.44	0.1016	0.0273	0.0522	0.0217
0.7	10^9	701^3	$(6.12 \pm 0.17) \times 10^3$	27.36 ± 0.67	0.0640	0.0198	0.0387	0.0186
5	10^7	257^3	$(1.52 \pm 0.02) \times 10^2$	7.82 ± 0.27	0.1211	0.0273	0.1172	0.0352
5	10^8	257^3	$(4.7 \pm 0.20) \times 10^2$	16.13 ± 0.56	0.0898	0.0273	0.0938	0.0273
5	10^9	513^3	$(1.47 \pm 0.04) \times 10^3$	30.06 ± 0.65	0.0559	0.0175	0.0664	0.0254
25	10^7	257^3	$(3.73 \pm 0.26) \times 10^1$	9.34 ± 0.18	0.1172	0.0273	0.1406	0.0508
25	10^8	257^3	$(1.16 \pm 0.07) \times 10^2$	16.91 ± 0.35	0.0859	0.0273	0.1211	0.0352
25	10^9	513^3	$(3.87 \pm 0.19) \times 10^2$	31.04 ± 0.71	0.0521	0.0166	0.1012	0.0311
50	10^7	257^3	$(1.88 \pm 0.05) \times 10^1$	9.17 ± 0.09	0.1172	0.0273	0.1406	0.0625
50	10^8	257^3	$(6.58 \pm 0.41) \times 10^1$	16.39 ± 0.22	0.0859	0.0273	0.1328	0.0469
50	10^9	513^3	$(1.98 \pm 0.03) \times 10^2$	31.08 ± 0.37	0.0484	0.0156	0.0965	0.0378
75	10^7	257^3	$(1.24 \pm 0.08) \times 10^1$	9.24 ± 0.25	0.1172	0.0273	0.1445	0.0742
75	10^8	257^3	$(4.10 \pm 0.03) \times 10^1$	17.35 ± 0.40	0.0859	0.0273	0.1211	0.0547
75	10^9	513^3	$(1.39 \pm 0.01) \times 10^2$	31.72 ± 0.37	0.0496	0.0156	0.1241	0.0413
100	10^7	257^3	9.36 ± 0.68	9.22 ± 0.17	0.1133	0.0273	0.1406	0.0703
100	10^8	257^3	$(3.09 \pm 0.19) \times 10^1$	17.47 ± 0.23	0.0820	0.0273	0.1016	0.0469
100	10^9	513^3	$(9.93 \pm 0.12) \times 10^1$	32.76 ± 0.87	0.0472	0.0146	0.1076	0.0436

(Nu), the thermal boundary layer thicknesses near the top and bottom boundaries (λ_T^t and λ_T^b, respectively), and the viscous boundary layer thicknesses near the top and bottom boundaries (λ_V^t and λ_V^b, respectively). We also report the associated errors in Re and Nu, with maximum errors of 20% and 18%, respectively, for 2D convection, and 7% and 6% for 3D convection. Simulations were conducted on Param Sanganak at IIT Kanpur and local laboratory clusters. Some of the simulations requiring higher grid resolutions were performed on Polaris at Argonne National Laboratory and on HPC cluster of the Kotak School of Sustainability at IIT Kanpur.

In the following three sections, we discuss the effect of Prandtl number on the flow structures, scaling of global quantities (Nu and Re), and the thermal and viscous boundary layers.

IV. VARIATION OF FLOW DYNAMICS WITH PRANDTL NUMBER

In this section, we explore the superadiabatic field profiles to understand variations in the flow structure, adiabatic temperature profiles, and the vertical field profiles to highlight the effect of Pr on the system.

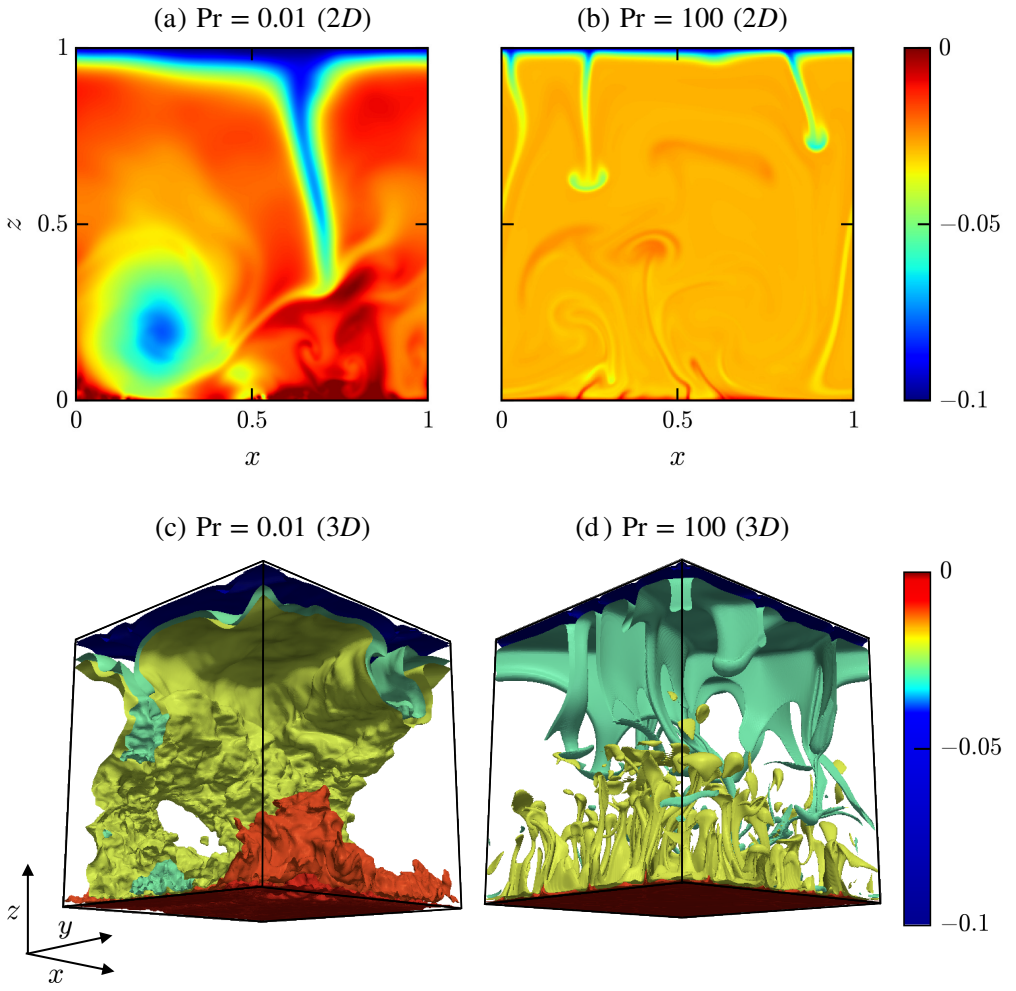

FIG. 2. Plots of the superadiabatic temperature $T_{\rm sa}(\mathbf{r})$ for (a), (c) Pr = 0.01 and (b), (d) Pr = 100 with Ra = 10^9. The top panel is for 2D and the bottom panel is for 3D. Hotter (red) and colder (blue) regions correspond to $T_{\rm sa} = 0$ and -0.1, respectively.

A. Flow structures

In compressible convection, the bulk flow is generally dominated by the adiabatic equilibrium profile [53,57]. As a result, using the total temperature field to visualize the flow can hide important details about the flow structures. Therefore, it is a standard practice to plot the superadiabatic temperature, $T_{\rm sa}(\mathbf{r})$ [Eq. (11)], for better visualization of the flow structures. The impact of the variation of Ra on these flow structures at Pr = 0.7 for turbulent compressible convection has already been discussed in detail by Tiwari *et al.* [53]. Here, we focus on the effect of Pr on the flow states at a fixed Ra = 10^9.

We plot the superadiabatic temperature profiles in Figs. 2(a) and 2(b) for 2D and Figs. 2(c) and 2(d) for 3D, at Pr = 0.01 and 100. Note that $T_{\rm sa}$ ranges from 0 to -0.1, with 0 and -0.1 representing the hotter (red) and colder (blue) regions, respectively. In both 2D and 3D, the bulk-averaged $T_{\rm sa}$ remains between -0.02 and -0.03, confirming that the bulk remains close to the

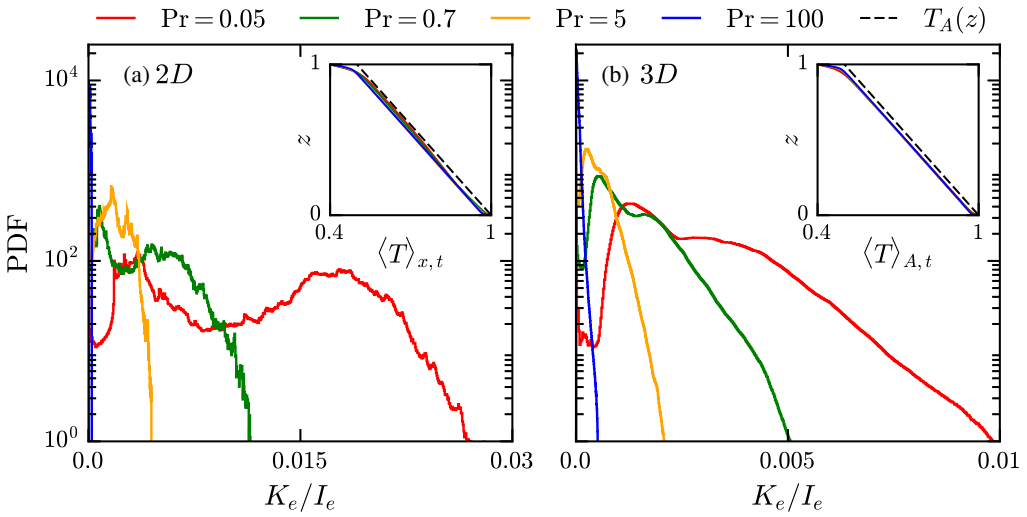

FIG. 3. Normalized probability distribution function (PDF) of the temporal averaged ratio of kinetic and internal energy, $r = K_e/I_e$, for (a) 2D and (b) 3D, with Pr = 0.05 (red), 0.7 (green), 5 (orange), and 100 (blue) at Ra = 10^9. The inset shows the spatiotemporal averaged temperature profiles, $\langle T \rangle_{x,t}$ in (a) for 2D and $\langle T \rangle_{A,t}$ in (b) for 3D; the black dashed line denotes the adiabatic temperature profile $T_A(z)$.

adiabatic equilibrium profile. This behavior contrasts with that of RBC, where the mean temperature is typically symmetric. For small Pr (Pr = 0.01), the flow is dominated by coherent large-scale structures, as seen in Figs. 2(a) and 2(c). As Pr increases, large-scale flow states becomes less prominent, and thin thermal plumes start emanating from both the top and bottom boundaries [see Figs. 2(b) and 2(d) at Pr = 100]. Similar phenomena have been widely reported in previous studies of RBC, both experimental and numerical [8,22].

Another notable feature that is observed in compressible convection is the asymmetry of the thermal boundary layers [52,53]. At low Pr (Pr = 0.01), the top thermal boundary layer is visibly thicker than the bottom one [Figs. 2(a) and 2(c)]. With the increase in Pr, both boundary layers become thinner. However, for large Pr as well, this asymmetry persists and the top boundary layer is thicker compared to the bottom one. We will discuss the details on the thermal boundary layer thicknesses and its scaling with both Ra and Pr in Sec. VI. In the next subsection, we examine the energetics and adiabatic temperature profiles.

B. Comparision of kinetic and internal energies

To examine the thermodynamic state of the system, we analyze the ratio of kinetic to internal energy, defined as

$$r = \frac{K_e}{I_e} = \frac{\rho u^2/2}{\rho C_V T}, \tag{16}$$

where K_e and I_e are the kinetic and internal energy densities, respectively. We compute this ratio at every spatial point and then perform a temporal average over 12 to 15 snapshots, spaced 5 time units apart, after the system reaches a statistically steady state. Figure 3 presents the normalized probability density function (PDF) of r for both 2D and 3D convection at Ra = 10^9, for Pr = 0.05, 0.7, 5, and 100. For all cases, we notice that $r \to 0$, indicating that internal energy vastly dominates over kinetic energy in most of the domain. This trend is especially pronounced at high Pr's, where the root-mean-square (rms) velocity—and consequently K_e—is small. As Pr decreases, the rms velocity increases, resulting in a larger K_e and hence an increase in r. For Pr = 0.05, we find

that $r \lessapprox 0.03$ in 2D and $\lessapprox 0.01$ in 3D, suggesting that significantly low Prandtl numbers are needed for kinetic energy to become comparable to internal energy. The value of r is smaller in 3D than in 2D because, in 2D convection, kinetic energy is concentrated in large-scale coherent motions due to the inverse energy cascade [68,69]. In contrast, in 3D, the energy cascades forward to smaller scales and is distributed among three velocity components, yielding a smaller kinetic-to-internal energy ratio.

Due to the dominance of internal energy over the kinetic energy in the bulk, the total temperature field exhibits a nearly linear vertical profile in the bulk, with a gradient that closely matches the adiabatic lapse rate, $-g/C_p$. This behavior is illustrated in the insets of Fig. 3, which show the horizontally and temporally averaged temperature profiles—$\langle T \rangle_{x,t}$ in 2D and $\langle T \rangle_{A,t}$ in 3D—for the same four Prandtl numbers. In all cases, the total temperature profiles closely follow the background adiabatic equilibrium profile $T_A(z) = 1 - (g/C_p)z$, indicated by the black dashed line. Deviations from this trend are confined to thin boundary layers near the walls. It is also worth noting that $\langle T \rangle_{x,t}$ and $\langle T \rangle_{A,t}$ remain largely insensitive to variations in Pr and closely follow the adiabatic profile, except for minor deviations at low Pr in 2D due to fluctuations [70], as shown in the insets of Fig. 3. These fluctuations arise in 2D at low Pr due to the absence of vortex stretching [71], which allows coherent large-scale structures to persist and modulate the mean temperature profile around $\langle T \rangle \approx 0.5$.

Next, we will discuss the vertical profiles of the temperature and density relative to their respective adiabatic counterparts.

C. Vertical profiles

In Sec. IV B, we showed that the bulk is mostly dominated by the adiabatic profile. Therefore, to highlight the effects of Pr on the temperature and density, we subtract the corresponding adiabatic profiles. We analyze the planar and temporal averaged superadiabatic temperature, $\langle T_{\rm sa} \rangle = \langle T - T_A(z) \rangle$, and the deviation of density from the adiabatic state, $\langle \rho - \rho_A(z) \rangle$. Note that these averages are obtained using 15 to 20 snapshots, with an interval of 5 time units.

Figure 4 shows the vertical profiles of these quantities, where the left and right columns correspond to the 2D and 3D cases, respectively, for Pr = 0.05, 0.7, 5, and 100, at $\mathrm{Ra} = 10^9$. As evident from Figs. 4(a) and 4(b), the superadiabatic temperature remains close to the adiabatic temperature with an average value around $\langle T_{\rm sa} \rangle \approx -0.025$ in the bulk, for both 2D and 3D. This observation is consistent with the field plots of $T_{\rm sa}$ presented earlier in Sec. IV A, and reflects the strong influence of the background adiabatic stratification that dominates the thermal structures in the bulk region. In 3D, we observe that the $T_{\rm sa}$ profiles nearly overlap for all Pr, indicating minimal Pr dependence in the bulk, except near the boundaries. In contrast, the 2D flows exhibit noticeable deviations from the adiabatic profile with varying Pr. Specifically, high-Pr flows show larger deviations from adiabaticity in the bulk compared to low-Pr flows. A pronounced asymmetry is also observed in the boundary layers, with stronger superadiabatic cooling near the top boundary compared to the bottom in all cases [52,53].

The density deviations, shown in Figs. 4(c) and 4(d), are similarly confined near the boundaries, while the bulk region remains close to the adiabatic profile. In both 2D and 3D simulations, the density variations are more pronounced near the bottom boundary than near the top boundary. This asymmetry was also reported in our earlier study examining the dependence of Ra at fixed Pr [53]. With varying Pr, we find that in the upper part of the bulk, density remains closer to the adiabatic profile, whereas in the lower bulk, larger deviations persist. Similar to the temperature profiles, in 3D, the profiles of $\langle \rho - \rho_A(z) \rangle$ for different Pr values collapse almost perfectly onto a single curve throughout most of the bulk, again indicating weak sensitivity to Pr in the turbulent interior. However, 2D flows show stronger fluctuations in density deviations. Specifically, low-Pr flows exhibit larger departures from adiabaticity in the upper bulk, while high-Pr flows show stronger deviations near the lower boundary.

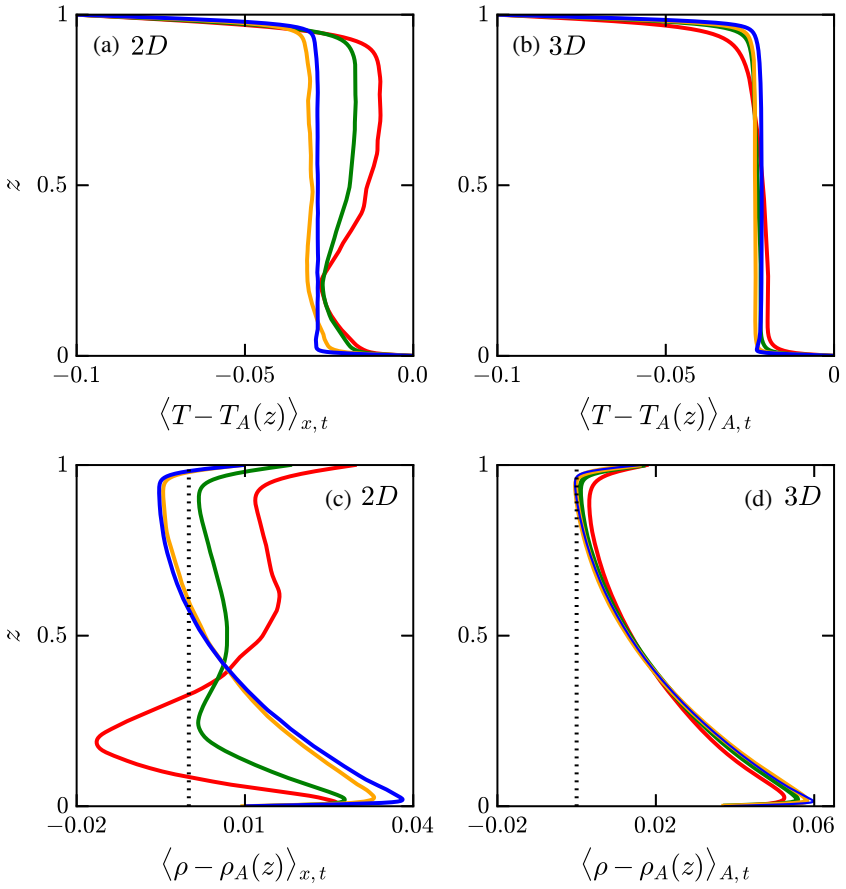

FIG. 4. Plots of the spatiotemporal averaged (a), (b) $\langle T_{\rm sa}(z)\rangle = \langle T - T_A(z)\rangle$ and (c), (d) $\langle \rho - \rho_A(z)\rangle$ at $\mathrm{Ra} = 10^9$. The left column is for 2D and right is for 3D. The color scheme is same as Fig. 3. The dotted black line represents the zero line.

Together with the results from varying Ra [53], these findings confirm that the asymmetry in both thermal and density structures is a robust and persistent feature of compressible convection. We now turn our attention to the scaling of global quantities.

V. SCALING OF THE NUSSELT AND REYNOLDS NUMBER

In this section, we compute the global quantities—the Nusselt number and the Reynolds number—and analyze their dependence on both Ra and Pr.

The Nusselt number (Nu) is computed using Eq. (13). Time averaging is performed over 2000 to 8000 data frames after the system reaches a statistically steady state. The computed Nu values, along with their standard errors, are listed in Tables I and II for the 2D and 3D simulations, respectively. From both tables, it is evident that Nu is consistently higher in 2D than in 3D for low-Pr cases. This difference may be attributed to the presence of the toroidal component of velocity in 3D flows—which is absent in 2D—and which increases kinetic energy at low Pr, thereby lowering Nu [63,64].

Earlier studies on RBC suggest that Nu follows distinct scaling laws in the low- and high-Pr regimes [26,34,38,63,72]. Therefore, to examine the Pr dependence of Nu in compressible convection, we also divide the analysis into two regimes: low-Pr ($\mathrm{Pr} < 1$) and high-Pr ($\mathrm{Pr} > 1$). In Fig. 5, we plot the compensated quantity $\mathrm{Nu}\mathrm{Ra}^{-\alpha}\mathrm{Pr}^{-\beta}$ as a function of Pr for $\mathrm{Ra} = 10^7$, 10^8, and 10^9. From

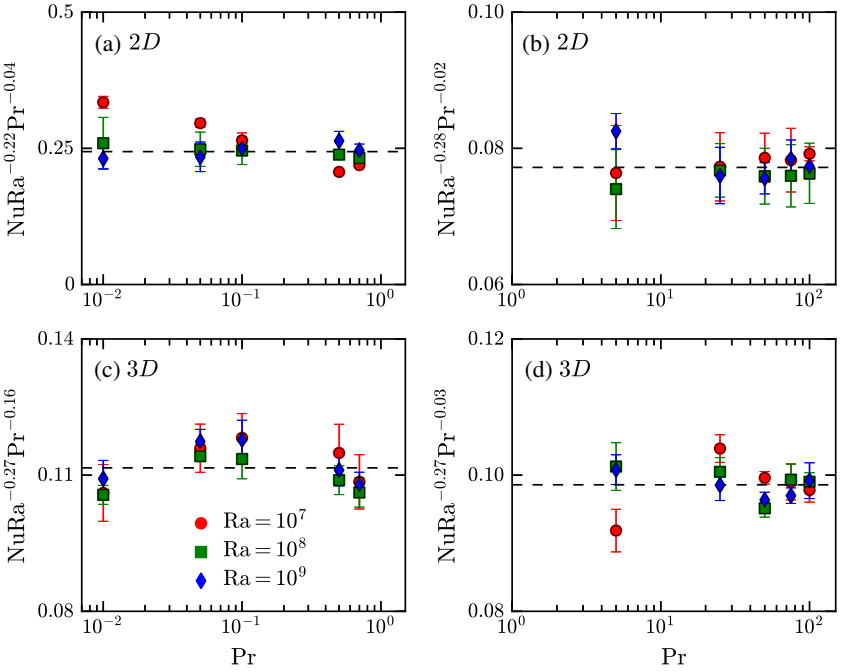

FIG. 5. Scaling of normalized Nu with Pr for (a), (c) Pr < 1 and (b), (d) Pr > 1. The top row (a), (b) shows 2D results, while the bottom row (c), (d) shows 3D results. The red circles, green squares, and blue diamonds correspond to Ra $= 10^7$, Ra $= 10^8$, and Ra $= 10^9$, respectively. Error bars represent the standard deviation in the time series of Nu at each Ra and Pr.

the figure, we observe that Nu increases with both Ra and Pr in the two regimes. For 2D convection, Nu exhibits a weak dependence on Pr in both regimes, as shown in Figs. 5(a) and 5(b) [63]. However, this dependence is slightly more pronounced for Pr < 1, due to the presence of large-scale coherent structures at low Pr. The Ra exponent increases slightly from Pr < 1 to Pr > 1, suggesting that heat transport becomes more efficient with increasing Ra, particularly for high-Pr fluids. Note that for 2D and Pr < 1, although the data points for Ra $= 10^7$ are shown in Fig. 5(a), they are excluded from the scaling fit due to larger discrepancies at that Ra. In contrast, the 3D convection data [Figs. 5(c) and 5(d)] reveal two distinct scaling regimes. For Pr < 1, Nu displays a strong dependence on both Ra and Pr; whereas for Pr > 1, while the Ra dependence remains comparable, the sensitivity to Pr is significantly weaker in this regime. The Nu scaling for both 2D and 3D convection in both regimes are reported in Table III.

The high heat transport observed at low-Pr values is due to the presence of large-scale flows, whereas at high-Pr, thermal plumes serve as the dominant mechanism for heat transport [8,22,64].

TABLE III. Scaling relations for the Nusselt number (Nu) and the Reynolds number (Re) with Ra and Pr for Pr < 1 and Pr > 1 in 2D and 3D convection.

Quantity	Dim	Pr < 1	Pr > 1
Nu	2D	$(0.24 \pm 0.07)\,\mathrm{Ra}^{0.22\pm0.01}\mathrm{Pr}^{0.04\pm0.01}$	$(0.077 \pm 0.006)\,\mathrm{Ra}^{0.28\pm0.004}\mathrm{Pr}^{0.02\pm0.007}$
Nu	3D	$(0.11 \pm 0.01)\,\mathrm{Ra}^{0.27\pm0.006}\mathrm{Pr}^{0.16\pm0.007}$	$(0.099 \pm 0.008)\,\mathrm{Ra}^{0.27\pm0.004}\mathrm{Pr}^{0.034\pm0.008}$
Re	2D	$(0.20 \pm 0.08)\,\mathrm{Ra}^{0.51\pm0.02}\mathrm{Pr}^{-0.78\pm0.03}$	$(0.05 \pm 0.006)\,\mathrm{Ra}^{0.60\pm0.006}\mathrm{Pr}^{-0.99\pm0.01}$
Re	3D	$(0.41 \pm 0.04)\,\mathrm{Ra}^{0.45\pm0.006}\mathrm{Pr}^{-0.64\pm0.007}$	$(0.17 \pm 0.02)\,\mathrm{Ra}^{0.51\pm0.007}\mathrm{Pr}^{-0.91\pm0.01}$

TABLE IV. Scaling of the volume-time averaged correlation $C(\rho u_z, T_{sa})$, root-mean-square values of ρu_z and T_{sa} with Pr in 2D and 3D at $\mathrm{Ra} = 10^7$, 10^8, and 10^9. Top: $\mathrm{Pr} < 1$, bottom: $\mathrm{Pr} > 1$.

Quantity	Dim	$\mathrm{Ra} = 10^7$	$\mathrm{Ra} = 10^8$	$\mathrm{Ra} = 10^9$
			$\mathrm{Pr} < 1$	
$C(\rho u_z, T_{sa})$	2D	$(0.08 \pm 0.003)\,\mathrm{Pr}^{-0.18\pm0.01}$	$(0.05 \pm 0.003)\,\mathrm{Pr}^{-0.11\pm0.02}$	$(0.02 \pm 0.001)\,\mathrm{Pr}^{-0.24\pm0.01}$
$\langle(\rho u_z)^2\rangle^{1/2}$	2D	$(0.10 \pm 0.007)\,\mathrm{Pr}^{-0.33\pm0.03}$	$(0.12 \pm 0.01)\,\mathrm{Pr}^{-0.24\pm0.04}$	$(0.14 \pm 0.004)\,\mathrm{Pr}^{-0.16\pm0.01}$
$\langle T_{sa}^2\rangle^{1/2}$	2D	$(0.029 \pm 0.001)\,\mathrm{Pr}^{-0.04\pm0.006}$	$(0.025 \pm 0.0004)\,\mathrm{Pr}^{-0.06\pm0.006}$	$(0.025 \pm 0.0003)\,\mathrm{Pr}^{-0.03\pm0.004}$
$C(\rho u_z, T_{sa})$	3D	$(0.14 \pm 0.007)\,\mathrm{Pr}^{-0.12\pm0.02}$	$(0.11 \pm 0.003)\,\mathrm{Pr}^{-0.16\pm0.01}$	$(0.08 \pm 0.005)\,\mathrm{Pr}^{-0.19\pm0.02}$
$\langle(\rho u_z)^2\rangle^{1/2}$	3D	$(0.07 \pm 0.003)\,\mathrm{Pr}^{-0.14\pm0.02}$	$(0.06 \pm 0.0003)\,\mathrm{Pr}^{-0.137\pm0.002}$	$(0.05 \pm 0.002)\,\mathrm{Pr}^{-0.13\pm0.01}$
$\langle T_{sa}^2\rangle^{1/2}$	3D	$(0.029 \pm 0.001)\,\mathrm{Pr}^{-0.05\pm0.01}$	$(0.028 \pm 0.0003)\,\mathrm{Pr}^{-0.03\pm0.004}$	$(0.026 \pm 0.0003)\,\mathrm{Pr}^{-0.02\pm0.004}$
			$\mathrm{Pr} > 1$	
$C(\rho u_z, T_{sa})$	2D	$(0.07 \pm 0.002)\,\mathrm{Pr}^{-0.02\pm0.01}$	$(0.04 \pm 0.001)\,\mathrm{Pr}^{0.003\pm0.008}$	$(0.02 \pm 0.001)\,\mathrm{Pr}^{0.023\pm0.014}$
$\langle(\rho u_z)^2\rangle^{1/2}$	2D	$(0.08 \pm 0.004)\,\mathrm{Pr}^{-0.44\pm0.02}$	$(0.11 \pm 0.004)\,\mathrm{Pr}^{-0.494\pm0.01}$	$(0.14 \pm 0.003)\,\mathrm{Pr}^{-0.498\pm0.005}$
$\langle T_{sa}^2\rangle^{1/2}$	2D	$(0.035 \pm 0.0005)\,\mathrm{Pr}^{-0.016\pm0.004}$	$(0.033 \pm 0.0006)\,\mathrm{Pr}^{-0.028\pm0.005}$	$(0.034 \pm 0.0006)\,\mathrm{Pr}^{-0.024\pm0.005}$
$C(\rho u_z, T_{sa})$	3D	$(0.10 \pm 0.008)\,\mathrm{Pr}^{-0.08\pm0.02}$	$(0.08 \pm 0.001)\,\mathrm{Pr}^{-0.13\pm0.03}$	$(0.06 \pm 0.001)\,\mathrm{Pr}^{-0.13\pm0.05}$
$\langle(\rho u_z)^2\rangle^{1/2}$	3D	$(0.093 \pm 0.001)\,\mathrm{Pr}^{-0.45\pm0.02}$	$(0.073 \pm 0.001)\,\mathrm{Pr}^{-0.37\pm0.04}$	$(0.07 \pm 0.001)\,\mathrm{Pr}^{-0.36\pm0.04}$
$\langle T_{sa}^2\rangle^{1/2}$	3D	$(0.032 \pm 0.0001)\,\mathrm{Pr}^{-0.01\pm0.001}$	$(0.028 \pm 0.0005)\,\mathrm{Pr}^{-0.011\pm0.005}$	$(0.027 \pm 0.0005)\,\mathrm{Pr}^{-0.01\pm0.005}$

Schmalzl *et al.* [63] first noted in 2D RBC that at $\mathrm{Ra} = 10^6$, Nu exhibited no significant variation across a broad Pr range of $10^{-2} \leqslant \mathrm{Pr} \leqslant 10^2$. We find that in our compressible simulations too, Nu does not vary much with Pr in 2D, even up to $\mathrm{Ra} = 10^9$. In 3D, it is also worth noting that the scaling exponents obtained are in good agreement with those reported for RBC [8,22,64,73].

From Eq. (12), since $\mathrm{Nu}_K \ll \mathrm{Nu}_{\mathrm{conv}}$ [53], we can approximate the *bulk* Nu as

$$\mathrm{Nu} \approx 1 + \frac{\sqrt{\mathrm{RaPr}}}{\epsilon}\langle \rho u_z T_{sa}\rangle_{V,t}. \tag{17}$$

Based on Eq. (17), one might expect Nu to scale as $\mathrm{Ra}^{0.5}\mathrm{Pr}^{0.5}$. However, our numerical results reveal deviations from this scaling, primarily due to the nontrivial dependence of the convective heat flux term $\langle \rho u_z T_{sa}\rangle_{V,t}$ on both Ra and Pr. To make this dependence explicit, we express the term as

$$\langle \rho u_z T_{sa}\rangle_{V,t} = C(\rho u_z, T_{sa})\langle(\rho u_z)^2\rangle_{V,t}^{1/2}\langle T_{sa}^2\rangle_{V,t}^{1/2}, \tag{18}$$

where $C(\rho u_z, T_{sa})$ is the normalized correlation between ρu_z and T_{sa} defined as

$$C(\rho u_z, T_{sa}) = \left\langle \frac{\langle \rho u_z T_{sa}\rangle_V}{\langle(\rho u_z)^2\rangle_V^{1/2}\langle T_{sa}^2\rangle_V^{1/2}} \right\rangle_t. \tag{19}$$

The scaling behaviors of the three terms in Eq. (18) with Pr are shown in Fig. 6 and with Ra are shown in Fig. 7. These quantities collectively determine the effective Pr and Ra dependence of Nu. The corresponding scaling exponents for each Ra are summarized in Table IV and for each Pr are summarized in Table V.

From the Fig. 6 and Table IV, we observe that each of the three terms—$C(\rho u_z, T_{sa})$, $\langle(\rho u_z)^2\rangle^{1/2}$, and $\langle T_{sa}^2\rangle^{1/2}$—decrease with increasing Pr and exhibit negative power-law scaling. Specifically, in the case of 2D for both $\mathrm{Pr} < 1$ and $\mathrm{Pr} > 1$, these factors themselves make up $\approx \mathrm{Pr}^{0.5}$, and therefore Nu follows a very weak scaling with Pr in both regimes. A similar cancellation is observed in 3D for $\mathrm{Pr} > 1$. However, for $\mathrm{Pr} < 1$, the combined scaling of the three components is approximately $\mathrm{Pr}^{0.32}$ leading to effective $\mathrm{Nu} \sim \mathrm{Pr}^{0.16}$ scaling. With Ra, the three terms collectively exhibit a decreasing trend as $\sim \mathrm{Ra}^{-0.28}$ for $\mathrm{Pr} < 1$ and $\sim \mathrm{Ra}^{-0.22}$ for $\mathrm{Pr} > 1$ in 2D, resulting in effective Nu scalings of $\sim \mathrm{Ra}^{-0.22}$ and $\sim \mathrm{Ra}^{-0.28}$, respectively. In 3D, the combined scaling is consistently $\sim \mathrm{Ra}^{-0.23}$ across

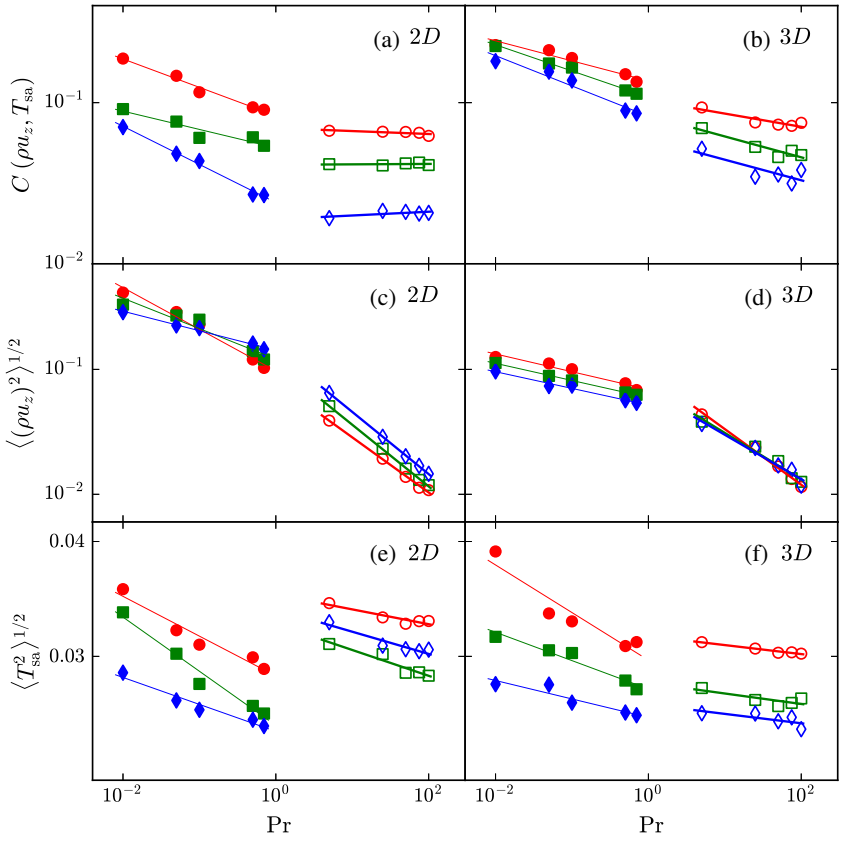

FIG. 6. Plots of the volume-time averaged (a), (b) $C(\rho u_z, T_{\rm sa})$, (c), (d) $\langle(\rho u_z)^2\rangle^{1/2}$, and (e), (f) $\langle T_{\rm sa}^2\rangle^{1/2}$ with Pr. The left column is for 2D and right is for 3D. Filled (empty) markers with thin (thick) lines are for Pr < 1 (Pr > 1). Color convention is same as Fig. 5.

both Pr regimes, leading to a corresponding Nu scaling of $\sim \mathrm{Ra}^{-0.27}$ (see Fig. 7 and Table V). Note that the scaling of these terms with Ra exhibit larger errors, particularly in 2D. This is primarily due to two factors: (i) the limited number of Rayleigh numbers (only three values) and (ii) the individual quantities exhibit significant fluctuations in 2D compared to 3D.

Next, we discuss the scaling of the Reynolds number with Ra and Pr. The Reynolds number (Re) is computed using Eq. (14), where the rms velocity U itself depends on both Ra and Pr, and determines the effective scaling of Re with Ra and Pr. We compute Re by taking the time average over 10 000 to 15 000 data frames and report these values in Table I for 2D and Table II for 3D, along with their respective errors. From the tables, we observe that Re is consistently higher in 2D than in 3D, especially at low Pr, likely due to reduced dissipation and stronger coherent structures in 2D flows [63,64].

Analogous to Nu, we analyze the scaling behavior of Re with Ra and Pr by plotting the compensated quantity $\mathrm{Re}\mathrm{Ra}^{-\delta}\mathrm{Pr}^{-\sigma}$ as a function of Pr in Fig. 8. We examine the scaling separately in the low-Pr and high-Pr regimes. Previous studies on RBC suggest that Re typically scales as -0.7 for Pr < 1, and decreases approximately linearly for large Pr [19,22,26,38,43,63,72]. The Ra-exponent in RBC usually lies between 0.4 and 0.6 depending on Pr [8,19,22,38,62,66].

In our compressible convection simulations, we observe similar trends as well. Re shows a strong dependence on both Ra and Pr, as presented in Fig. 8 and Table III. For both 2D and 3D convection, Re increases significantly with Ra, with slightly higher Ra exponents at larger Pr, consistent with

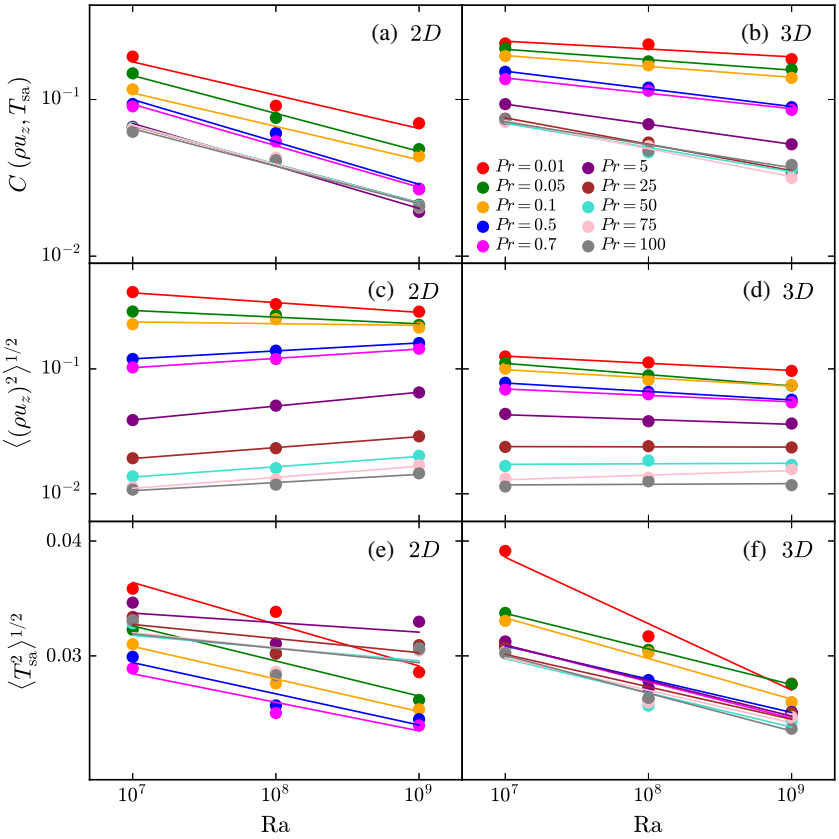

FIG. 7. Plots of the volume-time averaged (a), (b) $C(\rho u_z, T_{\rm sa})$, (c), (d) $\langle(\rho u_z)^2\rangle^{1/2}$, and (e), (f) $\langle T_{\rm sa}^2\rangle^{1/2}$ with Ra for different Pr's. The left column is for 2D and right is for 3D.

prior RBC studies [8,19,38,66]. The Ra exponent in case of 2D is also higher compared to the case of 3D across both Pr regimes [64]. Conversely, Re decreases with increasing Pr, more rapidly for high-Pr compared to low-Pr, indicating that viscous effects suppress the flow velocity in high-Pr fluids. This inverse Pr dependence is more pronounced in 2D compared to 3D [38,63,64].

We note that combined scaling relations for both Nu and Re are well established for RBC but not for compressible convection. The prefactors obtained in the present study are consistently smaller than those reported for RBC in both 2D and 3D [19,61,66,74], indicating reduced heat and momentum transport efficiency in the presence of compressibility. This trend is consistent with a previous comparative study, where the prefactors for RBC were found to be systematically larger than those for compressible convection in both 2D and 3D [74].

VI. PRANDTL DEPENDENCE OF THE BOUNDARY LAYER

We now shift our focus from the bulk to the boundaries. As noted in the discussion of temperature profiles in Sec. IV, we find that the temperature drops rather sharply near the top and bottom walls. To better understand the influence of the Prandtl number on the boundary layers, we now examine their structure in more detail. First, we discuss the thermal boundary layers.

Figure 9 shows the zoomed-in profiles of $\langle T\rangle_{x,t}$ for 2D and $\langle T\rangle_{A,t}$ for 3D, near the top and bottom boundaries, for Pr $= 0.05,\ 0.7,\ 5,\ 100$ at Ra $= 10^9$. Unlike the bulk region, where the temperature profile remains nearly independent of Pr, the thermal structure near the boundaries displays a strong sensitivity to Pr. It is evident from the figure that an increase in Pr results in gradual thinning of

TABLE V. Scaling of the volume-time averaged correlation $C(\rho u_z, T_{sa})$, root-mean-square values of ρu_z and T_{sa} with Ra for different Pr. Top: 2D, bottom: 3D.

Pr	$C(\rho u_z, T_{sa})$	$\langle(\rho u_z)^2\rangle^{1/2}$	$\langle T_{sa}^2\rangle^{1/2}$
		2D	
0.01	$(5.35 \pm 5.80)\,\mathrm{Ra}^{-0.21\pm0.06}$	$(1.44 \pm 0.28)\,\mathrm{Ra}^{-0.078\pm0.010}$	$(0.075 \pm 0.016)\,\mathrm{Ra}^{-0.045\pm0.012}$
0.05	$(7.00 \pm 3.20)\,\mathrm{Ra}^{-0.24\pm0.02}$	$(0.70 \pm 0.19)\,\mathrm{Ra}^{-0.053\pm0.015}$	$(0.060 \pm 0.008)\,\mathrm{Ra}^{-0.038\pm0.007}$
0.1	$(3.42 \pm 2.50)\,\mathrm{Ra}^{-0.21\pm0.04}$	$(0.30 \pm 0.17)\,\mathrm{Ra}^{-0.014\pm0.031}$	$(0.054 \pm 0.004)\,\mathrm{Ra}^{-0.035\pm0.004}$
0.5	$(7.81 \pm 7.10)\,\mathrm{Ra}^{-0.27\pm0.05}$	$(0.043 \pm 0.001)\,\mathrm{Ra}^{0.064\pm0.002}$	$(0.051 \pm 0.010)\,\mathrm{Ra}^{-0.034\pm0.011}$
0.7	$(6.64 \pm 2.90)\,\mathrm{Ra}^{-0.27\pm0.02}$	$(0.031 \pm 0.003)\,\mathrm{Ra}^{0.075\pm0.004}$	$(0.047 \pm 0.009)\,\mathrm{Ra}^{-0.031\pm0.010}$
5	$(5.56 \pm 3.80)\,\mathrm{Ra}^{-0.27\pm0.04}$	$(0.0066 \pm 0.0004)\,\mathrm{Ra}^{0.111\pm0.003}$	$(0.039 \pm 0.014)\,\mathrm{Ra}^{-0.010\pm0.020}$
25	$(3.55 \pm 1.40)\,\mathrm{Ra}^{-0.25\pm0.02}$	$(0.0047 \pm 0.0004)\,\mathrm{Ra}^{0.088\pm0.004}$	$(0.041 \pm 0.011)\,\mathrm{Ra}^{-0.015\pm0.014}$
50	$(3.73 \pm 2.10)\,\mathrm{Ra}^{-0.25\pm0.03}$	$(0.0036 \pm 0.0006)\,\mathrm{Ra}^{0.083\pm0.009}$	$(0.039 \pm 0.017)\,\mathrm{Ra}^{-0.014\pm0.023}$
75	$(3.88 \pm 2.70)\,\mathrm{Ra}^{-0.25\pm0.04}$	$(0.0027 \pm 0.0007)\,\mathrm{Ra}^{0.088\pm0.014}$	$(0.041 \pm 0.017)\,\mathrm{Ra}^{-0.016\pm0.023}$
100	$(3.06 \pm 1.90)\,\mathrm{Ra}^{-0.24\pm0.03}$	$(0.004 \pm 0.001)\,\mathrm{Ra}^{0.065\pm0.014}$	$(0.041 \pm 0.019)\,\mathrm{Ra}^{-0.016\pm0.025}$
		3D	
0.01	$(0.53 \pm 0.25)\,\mathrm{Ra}^{-0.050\pm0.025}$	$(0.32 \pm 0.03)\,\mathrm{Ra}^{-0.058\pm0.006}$	$(0.12 \pm 0.03)\,\mathrm{Ra}^{-0.072\pm0.012}$
0.05	$(0.61 \pm 0.10)\,\mathrm{Ra}^{-0.066\pm0.009}$	$(0.47 \pm 0.05)\,\mathrm{Ra}^{-0.090\pm0.005}$	$(0.062 \pm 0.001)\,\mathrm{Ra}^{-0.039\pm0.001}$
0.1	$(0.59 \pm 0.07)\,\mathrm{Ra}^{-0.070\pm0.006}$	$(0.28 \pm 0.07)\,\mathrm{Ra}^{-0.066\pm0.014}$	$(0.067 \pm 0.007)\,\mathrm{Ra}^{-0.044\pm0.006}$
0.5	$(0.93 \pm 0.12)\,\mathrm{Ra}^{-0.113\pm0.007}$	$(0.23 \pm 0.01)\,\mathrm{Ra}^{-0.068\pm0.003}$	$(0.055 \pm 0.001)\,\mathrm{Ra}^{-0.036\pm0.001}$
0.7	$(0.67 \pm 0.17)\,\mathrm{Ra}^{-0.098\pm0.014}$	$(0.16 \pm 0.02)\,\mathrm{Ra}^{-0.051\pm0.008}$	$(0.058 \pm 0.007)\,\mathrm{Ra}^{-0.040\pm0.007}$
5	$(0.74 \pm 0.001)\,\mathrm{Ra}^{-0.128\pm0.000}$	$(0.080 \pm 0.017)\,\mathrm{Ra}^{-0.038\pm0.012}$	$(0.057 \pm 0.007)\,\mathrm{Ra}^{-0.039\pm0.006}$
25	$(1.15 \pm 0.21)\,\mathrm{Ra}^{-0.17\pm0.01}$	$(0.025 \pm 0.002)\,\mathrm{Ra}^{-0.002\pm0.005}$	$(0.053 \pm 0.012)\,\mathrm{Ra}^{-0.035\pm0.012}$
50	$(0.85 \pm 0.42)\,\mathrm{Ra}^{-0.16\pm0.03}$	$(0.016 \pm 0.007)\,\mathrm{Ra}^{0.004\pm0.023}$	$(0.054 \pm 0.012)\,\mathrm{Ra}^{-0.037\pm0.012}$
75	$(1.31 \pm 0.34)\,\mathrm{Ra}^{-0.18\pm0.01}$	$(0.007 \pm 0.002)\,\mathrm{Ra}^{0.037\pm0.018}$	$(0.053 \pm 0.011)\,\mathrm{Ra}^{-0.035\pm0.011}$
100	$(0.76 \pm 0.44)\,\mathrm{Ra}^{-0.15\pm0.03}$	$(0.011 \pm 0.004)\,\mathrm{Ra}^{0.005\pm0.021}$	$(0.058 \pm 0.005)\,\mathrm{Ra}^{-0.041\pm0.004}$

the thermal boundary layers [22,26,28,53]. This trend is observed consistently at both the top and bottom boundaries in both 2D and 3D simulations. Moreover, for a given Ra and Pr, the thermal boundary layer near the top wall is thicker than that near the bottom wall. This asymmetry between the top and bottom layers is a distinctive feature of compressible convection and arises due to the stratification of the fluid [52,53]. In particular, the thermal diffusivity κ is higher near the top wall than near the bottom, which results in broader thermal gradients and hence a thicker boundary layer at the top.

We now extend this qualitative discussion with a quantitative analysis by computing the thicknesses of the thermal boundary layers at the top and bottom. Note that the dependence of these thicknesses on Ra has already been discussed by Tiwari *et al.* [53] for fixed Pr = 0.7. Here, we explore their combined dependence on both Ra and Pr. As mentioned in Sec. IV B, the temperature profile in the bulk exhibits superadiabatic cooling, with its slope closely approximating the adiabatic temperature gradient $D = -0.5$. To determine the top and bottom thermal boundary layer thicknesses, λ_T^t and λ_T^b, we locate the grid points where the slope of $\langle T\rangle_{A,t}$ approaches $D = -0.5$. The computed values of λ_T^t and λ_T^b are listed in Tables I and II for the 2D and 3D simulations, respectively. As evident from the tables, λ_T^t consistently exceeds λ_T^b across all Ra and Pr.

To highlight the scaling behavior, we plot the normalized thermal boundary layer thicknesses, $\tilde{\lambda}_T^{t,b} = \lambda_T^{t,b}\mathrm{Ra}^{-\chi}\mathrm{Pr}^{-\zeta}$, as functions of Pr for the 2D and 3D simulations in Fig. 10. The left and right y axes in the figure correspond to the axes for the thicknesses of top and bottom thermal boundary layers, respectively. The color scheme follows that of Fig. 5; the solid and hollow markers represent the top and bottom thermal boundary layer thicknesses, respectively. In all cases, the prefactor of $\tilde{\lambda}_T^t$ is larger than that of $\tilde{\lambda}_T^b$, reaffirming that the top thermal boundary layer is consistently thicker than the bottom one. This is a characteristic feature of compressible convection [52,53]. Moreover, the

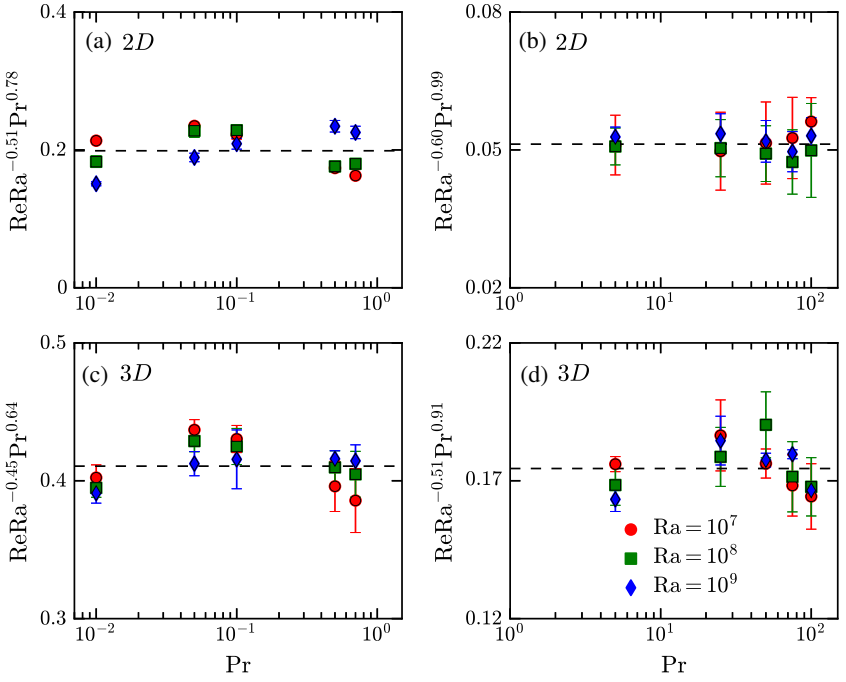

FIG. 8. Scaling of normalized Re with Pr for (a), (c) Pr $<$ 1 and (b), (d) Pr $>$ 1. The top panel (a), (b) is for 2D, while the bottom panel (c), (d) is for 3D. Color convention follows that of Fig. 5. Error bars represent the standard deviation in the time series of Re at each Ra and Pr.

scaling exponents for the top and bottom boundaries are distinct, which is in contrast to the identical scaling observed in RBC [75].

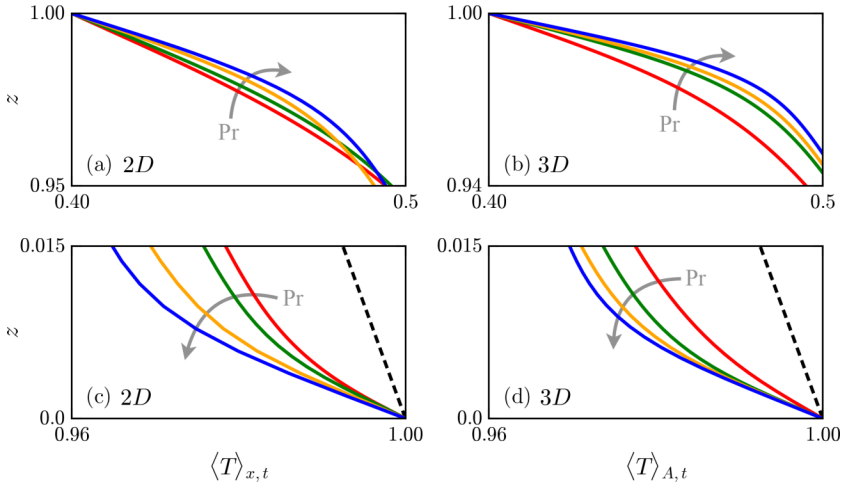

FIG. 9. Zoomed-in plots of (a), (c) $\langle T \rangle_{x,t}$ for 2D and (b), (d) $\langle T \rangle_{A,t}$ for 3D, shown near the top boundaries (a), (b) and the bottom boundaries (c), (d). The same color convention for different Pr's is used as in Fig. 3, with gray arrows indicating increasing Pr.

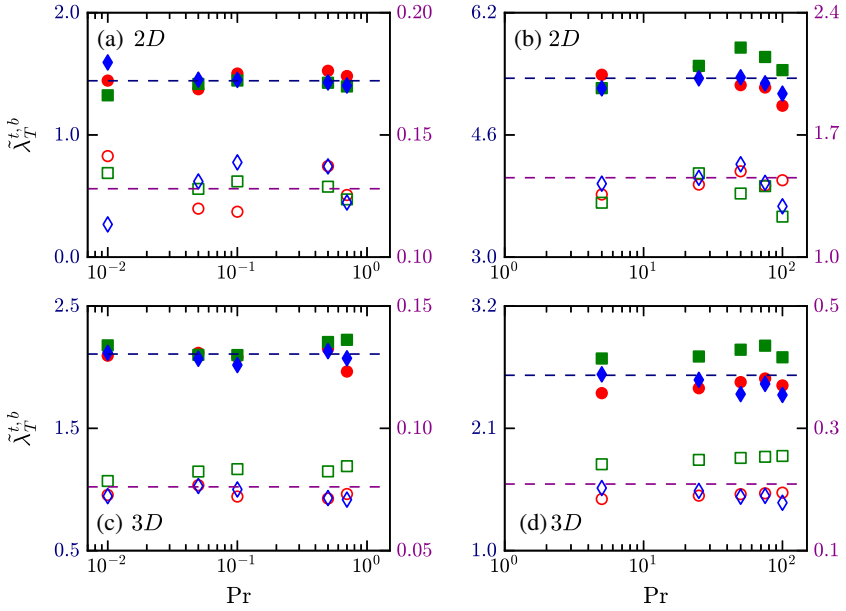

FIG. 10. Plots of normalized thermal boundary layer thicknesses $\tilde{\lambda}_T^{t,b}$ with Pr for (a), (c) Pr < 1 and (b), (d) Pr > 1. The top panel (a), (b) is for 2D, and the bottom panel (c), (d) is for 3D. Color coding is same as Fig. 5; the solid and hollow markers are for the top and bottom thermal boundary layer thicknesses. The left and right y axes represent the axes for thicknesses of the top and bottom thermal boundary layers, respectively.

The scaling relations of the thermal boundary layer thicknesses for 2D convection are

$$\lambda_T^t = \begin{cases} (1.44 \pm 0.18)\mathrm{Ra}^{-0.14\pm0.007}\mathrm{Pr}^{-0.09\pm0.008} & \text{if Pr} < 1 \\ (5.34 \pm 0.56)\mathrm{Ra}^{-0.22\pm0.01}\mathrm{Pr}^{-0.061\pm0.01} & \text{if Pr} > 1 \end{cases}, \tag{20}$$

$$\lambda_T^b = \begin{cases} (0.13 \pm 0.023)\mathrm{Ra}^{-0.098\pm0.01}\mathrm{Pr}^{-0.13\pm0.01} & \text{if Pr} < 1 \\ (1.40 \pm 0.23)\mathrm{Ra}^{-0.20\pm0.01}\mathrm{Pr}^{-0.075\pm0.015} & \text{if Pr} > 1 \end{cases}. \tag{21}$$

The scaling relations of the thermal boundary layer thicknesses for 3D convection are

$$\lambda_T^t = \begin{cases} (2.11 \pm 0.19)\mathrm{Ra}^{-0.17\pm0.005}\mathrm{Pr}^{-0.14\pm0.006} & \text{if Pr} < 1 \\ (2.58 \pm 0.43)\mathrm{Ra}^{-0.18\pm0.008}\mathrm{Pr}^{-0.032\pm0.015} & \text{if Pr} > 1 \end{cases}, \tag{22}$$

$$\lambda_T^b = \begin{cases} (0.076 \pm 0.013)\mathrm{Ra}^{-0.063\pm0.01}\mathrm{Pr}^{-0.076\pm0.011} & \text{if Pr} < 1 \\ (0.21 \pm 0.08)\mathrm{Ra}^{-0.12\pm0.02}\mathrm{Pr}^{-0.018\pm0.035} & \text{if Pr} > 1 \end{cases}. \tag{23}$$

The Ra dependence in both 2D and 3D is consistent with the findings of Tiwari *et al.* [53]: the top thermal boundary layer exhibits a steeper temperature gradient with increasing Ra compared to the bottom boundary. However, the Pr dependence exhibits contrasting behavior between 2D and 3D. In 2D, the bottom boundary shows a stronger Pr dependence, with steeper gradients than the top for both Pr < 1 and Pr > 1. In contrast, in 3D, it is the top boundary that exhibits a more pronounced variation with Pr, while the bottom boundary shows a weaker dependence. Furthermore, we find that for Pr > 1, the scaling exponents are smaller than those for Pr < 1, indicating that the influence of Pr on the thermal boundary layer thicknesses weakens with increasing Pr and can saturate for high Prandtl numbers [26].

We also discuss the influence of Pr on the viscous boundary layers across different Ra and Pr. Figure 11 shows the vertical profiles of the temporal averaged horizontal rms velocity, calculated as $U_h = \sqrt{\langle u_x^2 \rangle}$ in 2D and $U_h = \sqrt{\langle u_x^2 + u_y^2 \rangle}$ in 3D, for $\mathrm{Ra} = 10^9$ and the same four Prandtl numbers ($\mathrm{Pr} = 0.05,\ 0.7,\ 5,\ 100$). These temporal averages are obtained over 15 to 20 snapshots, taken at

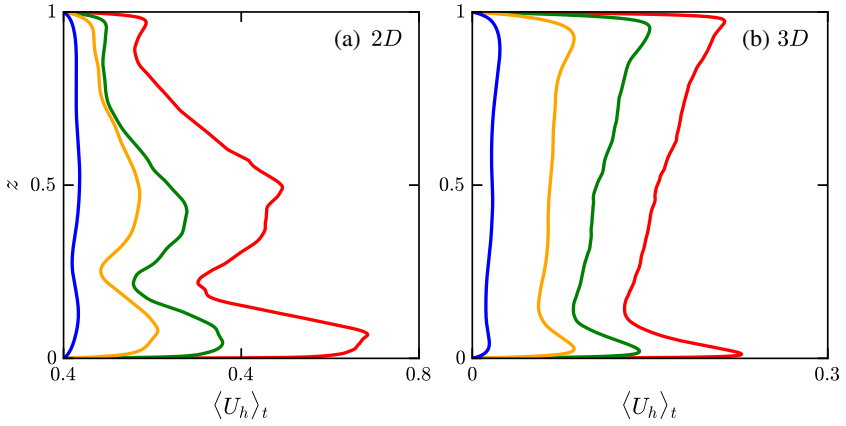

FIG. 11. Plots of the temporal averaged horizontal root-mean-square velocity U_h for (a) 2D and (b) 3D with $\mathrm{Ra} = 10^9$. Color convention is same as Fig. 3.

intervals of 5 time units. As seen in the figure, U_h displays clear local maxima near both the top and bottom boundaries. We define the viscous boundary layer thickness as the distance from the wall to the location of this local maximum. As Pr increases, these peaks shift farther away from the walls, indicating a thickening of the viscous boundary layers with increasing Pr. This trend is consistent with previous studies on RBC [19,22,26,28,65]. However, unlike RBC, compressible convection exhibits vertical asymmetry: the top viscous boundary layer is consistently thicker than the bottom one, similar to the behavior observed for the thermal boundary layers.

We calculate the thicknesses of the velocity boundary layers, λ_V^t and λ_V^b, near the top and bottom boundaries for each Ra and Pr. The computed values, listed in Table I for 2D and Table II for 3D, show that $\lambda_V^t > \lambda_V^b$ for all Ra and Pr. Also note that for $\mathrm{Pr} < 1$, the thermal boundary layer is thicker than the viscous one, while for $\mathrm{Pr} > 1$, the viscous layer dominates. Figure 12 displays the scaling of the normalized viscous boundary layer thicknesses, $\tilde{\lambda}_V^{t,b} = \lambda_V^{t,b}\mathrm{Ra}^{-\xi}\mathrm{Pr}^{-\eta}$, with Pr for both 2D and 3D convection. The color scheme is similar to Fig. 10. As shown in the figure, the prefactor of $\tilde{\lambda}_V^t$ is larger than that of $\tilde{\lambda}_V^b$ in all cases, implying that the viscous boundary layer is thicker near the top boundary compared to the bottom one.

The scaling relations of the viscous boundary layer thicknesses for 2D convection are

$$\lambda_V^t = \begin{cases} (2.1 \pm 0.5)\mathrm{Ra}^{-0.19\pm0.01}\mathrm{Pr}^{0.10\pm0.01} & \text{if } \mathrm{Pr} < 1 \\ (0.25 \pm 0.11)\mathrm{Ra}^{-0.07\pm0.02}\mathrm{Pr}^{0.17\pm0.04} & \text{if } \mathrm{Pr} > 1, \end{cases} \tag{24}$$

$$\lambda_V^b = \begin{cases} (0.11 \pm 0.04)\mathrm{Ra}^{-0.09\pm0.02}\mathrm{Pr}^{0.07\pm0.02} & \text{if } \mathrm{Pr} < 1 \\ (0.03 \pm 0.02)\mathrm{Ra}^{-0.02\pm0.04}\mathrm{Pr}^{0.18\pm0.07} & \text{if } \mathrm{Pr} > 1. \end{cases} \tag{25}$$

The scaling relations of the viscous boundary layer thicknesses for 3D convection are

$$\lambda_V^t = \begin{cases} (1.83 \pm 0.27)\mathrm{Ra}^{-0.19\pm0.01}\mathrm{Pr}^{0.10\pm0.01} & \text{if } \mathrm{Pr} < 1 \\ (0.31 \pm 0.09)\mathrm{Ra}^{-0.07\pm0.01}\mathrm{Pr}^{0.10\pm0.03} & \text{if } \mathrm{Pr} > 1, \end{cases} \tag{26}$$

$$\lambda_V^b = \begin{cases} (0.16 \pm 0.05)\mathrm{Ra}^{-0.11\pm0.02}\mathrm{Pr}^{0.15\pm0.02} & \text{if } \mathrm{Pr} < 1 \\ (0.14 \pm 0.03)\mathrm{Ra}^{-0.11\pm0.01}\mathrm{Pr}^{0.22\pm0.02} & \text{if } \mathrm{Pr} > 1. \end{cases} \tag{27}$$

We find that, in compressible convection as well, $\lambda_V^{t,b}$ increases with Pr and decreases with Ra, consistent with earlier studies on RBC [8,19,22,26,65]. Note that the magnitude of scaling exponent for Ra is higher for $\mathrm{Pr} < 1$ compared to $\mathrm{Pr} > 1$ in all cases, indicating that the viscous boundary layer thickness decreases more rapidly with Ra at low Pr. In contrast, the scaling exponents for Pr are larger for $\mathrm{Pr} > 1$ than for $\mathrm{Pr} < 1$, which implies a steeper increase in the viscous boundary layer thicknesses with Pr for $\mathrm{Pr} > 1$. Moreover, the thickness of top viscous boundary layer decreases

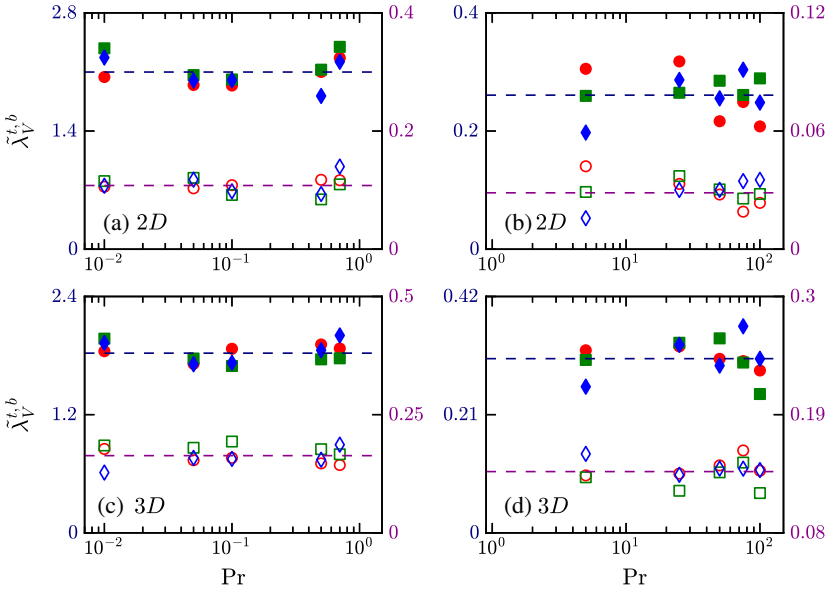

FIG. 12. Plots of normalized viscous boundary layer thicknesses $\tilde{\lambda}_V^{t,b}$ with Pr for (a), (c) Pr < 1 and (b), (d) Pr > 1. The top panel (a), (b) is for 2D, and the bottom panel (c), (d) is for 3D. Color convention is same as Fig. 10.

faster with Ra than the bottom boundary layers in both the low-Pr and high-Pr regimes. With Pr, the bottom boundary layer thickness increases faster than the top in 3D for both regimes. A similar trend is observed in 2D for Pr > 1, while for Pr < 1, the top viscous boundary layer increases slightly faster than the bottom one.

VII. CONCLUSIONS

In this paper, we present the results of extensive 2D and 3D numerical simulations to investigate the influence of the Prandtl number (Pr) on turbulent compressible convection. We conducted a total of 60 simulation runs in 2D and 3D, varying the Rayleigh number, Ra, and Pr in the range: Ra $= 10^7, 10^8, 10^9$ and $0.01 \leqslant$ Pr $\leqslant 100$ to cover a wide range of complex fluids. While a comprehensive study of the dependence of Ra and Pr on various quantities exists on RBC, the same for turbulent compressible convection is very limited. Our work makes a significant contribution in this direction.

We investigate several key aspects of the problem, including the effect of Pr on flow structures, energetics, vertical field profiles, scaling of global quantities, and boundary layer dynamics. Due to compressibility, the density is higher near the bottom boundary than the top, resulting in asymmetric dynamics that differ from the symmetric behavior observed in RBC. Despite this, our simulations reveal that some features observed in RBC—such as large-scale circulations at low Pr and long-tailed plumes at high Pr—also appear in compressible convection. However, due to the presence of an adiabatic background profile, compressible convection exhibits distinct behavior. The internal energy consistently dominates over the kinetic energy across all Prandtl numbers and the total temperature closely follows the adiabatic profile in the bulk, leading to an asymmetry in the mean temperature distribution. Although the flow structures may resemble those in RBC, adiabatic cooling shifts the superadiabatic temperature field toward the hotter side in the bulk—a contrast to RBC, where the mean temperature profile is symmetric.

The deviations of both temperature and density from their respective adiabatic profiles are smallest at the lowest Pr and largest at the highest Pr considered in 2D simulations, indicating a stronger departure from adiabaticity at higher Pr. In contrast, these deviations in 3D show minimal dependence on Pr. The Nusselt number, Nu, exhibits a very weak Pr dependence in 2D for both $\mathrm{Pr} < 1$ and $\mathrm{Pr} > 1$. In 3D, Nu increases with Pr for $\mathrm{Pr} < 1$, approximately as $\sim \mathrm{Pr}^{0.16}$, and shows only a weak variation for $\mathrm{Pr} > 1$. The Ra exponent in 2D increases slightly from $\sim \mathrm{Ra}^{0.22}$ for $\mathrm{Pr} < 1$ to $\sim \mathrm{Ra}^{0.28}$ for $\mathrm{Pr} > 1$, whereas in 3D it remains nearly constant $\sim \mathrm{Ra}^{0.27}$. The combined scaling of the normalized correlation along with the root-mean-square values of ρu_z and T_{sa} leads to a reduction of Nu from the theoretical prediction of $\mathrm{Nu} \sim \mathrm{Ra}^{0.5}\mathrm{Pr}^{0.5}$. The Reynolds number shows a strong dependence on Pr, scaling approximately as $\sim \mathrm{Pr}^{0.7}$ and $\sim \mathrm{Pr}^{0.95}$ for $\mathrm{Pr} < 1$ and $\mathrm{Pr} > 1$, respectively. The Ra exponent is higher for 2D than in 3D, and also higher for $\mathrm{Pr} < 1$ compared to $\mathrm{Pr} > 1$.

The boundary layers display a pronounced top-bottom asymmetry, with the top boundary layer consistently thicker than the bottom one across all Pr. The thicknesses of both the top and bottom thermal boundary layers decrease with increasing Pr, while the velocity boundary layer thicknesses increase with Pr. The thermal boundary layers exhibit a steeper Pr dependence for $\mathrm{Pr} < 1$ than for $\mathrm{Pr} > 1$, whereas the opposite trend is observed for the viscous boundary layer, with a steeper scaling for $\mathrm{Pr} > 1$. Correspondingly, the Ra exponents is larger for $\mathrm{Pr} > 1$ in the thermal boundary layers, but larger for $\mathrm{Pr} < 1$ in the viscous boundary layers. In addition, we find that the top and bottom boundary layers follow distinct scaling laws with Ra and Pr, highlighting asymmetry not only in structure but also in scaling behavior.

Overall, our study provides a detailed characterization of turbulent compressible convection across a wide range of Prandtl and Rayleigh numbers in both two and three dimensions. These findings deepen our understanding of stratified convection and can have important implications for modeling convection in geophysical and astrophysical systems. Future work could investigate the influence of varying stratification, or the role of compressibility in multiscale energy transfer. Additionally, exploring the effects of rotation, magnetic field, and boundary conditions could help extend the relevance of these findings to more realistic natural systems.

ACKNOWLEDGMENTS

The authors thank Shashwat Bhattacharya, Roshan Samuel, and Dhananjay Singh for their valuable comments and suggestions. Most of the simulations were performed on Param Sanganak at IIT Kanpur and local clusters, while simulations requiring higher grid resolution were conducted on Polaris at the Argonne Leadership Computing Facility (ALCF) through the Director's Discretionary Program, and on the HPC cluster of Kotak School of Sustainability (KSS), IIT Kanpur. L.S. thanks IIT Kanpur for the Institute Postdoctoral Fellowship. This work was partially supported by the Anusandhan National Research Foundation, India (Grant No. SERB/PHY/2021522), and the J. C. Bose Fellowship (Grant No. SERB/PHY/2023488).

DATA AVAILABILITY

The data that support the findings of this article are openly available [76].

APPENDIX: COMPARISON BETWEEN MACCORMACK-TVD AND OTHER SCHEMES

To assess the sensitivity of our results to the numerical scheme, we performed additional simulations using a third-order Central weighted essentially nonoscillatory (CWENO3) scheme and compared them with those obtained using the second-order MacCormack-TVD scheme employed in the main text. Both schemes were implemented with identical conditions and grid resolution at $\mathrm{Ra} = 10^9$ and $\mathrm{Pr} = 0.1$, while keeping other parameters fixed.

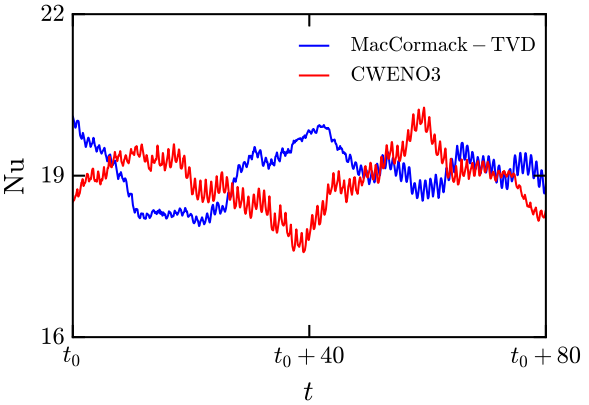

FIG. 13. Temporal evolution of Nu using the MacCormack-TVD scheme (blue) and CWENO3 scheme (red) at $\mathrm{Ra} = 10^9$ and $\mathrm{Pr} = 0.1$ for 2D convection. Both schemes yield similar results.

Figure 13 shows the temporal evolution of the Nusselt number, Nu, computed using both schemes. The time-averaged values are $\mathrm{Nu} = 19.69 \pm 0.75$ for the MacCormack–TVD scheme and $\mathrm{Nu} = 18.95 \pm 0.51$ for the CWENO3 scheme. These results demonstrate that the MacCormack-TVD scheme provides quantitatively consistent results with the higher-order CWENO3 scheme, confirming that the conclusions reported in the main text are robust and independent of the numerical scheme.

In addition, our code has been validated in a previous study [53] where the computed Nu and Re differed by less than 3% from those reported by John and Schumacher [57]. They employed a sixth-order compact finite-difference scheme for spatial derivatives (with lower-order treatments near the walls), confirming that our second-order MacCormack-TVD scheme yields quantitatively consistent results for similar convection setups. This close agreement is expected, because large-scale global quantities such as Nu and Re are relatively insensitive to the local order of numerical discretization.

[1] E. D. Siggia, High Rayleigh number convection, Annu. Rev. Fluid Mech. **26**, 137 (1994).
[2] G. Ahlers, S. Grossmann, and D. Lohse, Heat transfer and large scale dynamics in turbulent Rayleigh-Bénard convection, Rev. Mod. Phys. **81**, 503 (2009).
[3] D. Lohse and K.-Q. Xia, Small-scale properties of turbulent Rayleigh–Bénard convection, Annu. Rev. Fluid Mech. **42**, 335 (2010).
[4] F. Chillà and J. Schumacher, New perspectives in turbulent Rayleigh-Bénard convection, Eur. Phys. J. E **35**, 58 (2012).
[5] J. Schumacher and K. R. Sreenivasan, Colloquium: Unusual dynamics of convection in the sun, Rev. Mod. Phys. **92**, 041001 (2020).
[6] J. Schmalzl, M. Breuer, and U. Hansen, The influence of the Prandtl number on the style of vigorous thermal convection, Geophys. Astrophys. Fluid Dyn. **96**, 381 (2002).
[7] E. M. King and J. M. Aurnou, Turbulent convection in liquid metal with and without rotation, Proc. Natl. Acad. Sci. **110**, 6688 (2013).
[8] R. Verzicco and R. Camussi, Prandtl number effects in convective turbulence, J. Fluid Mech. **383**, 55 (1999).
[9] X. Liu and S. Zhong, Analyses of marginal stability, heat transfer and boundary layer properties for thermal convection in a compressible fluid with infinite Prandtl number, Geophys. J. Int. **194**, 125 (2013).

[10] M. K. Verma, *Physics of Buoyant Flows: From Instabilities to Turbulence* (World Scientific, Singapore, 2018).
[11] E. A. Spiegel and G. Veronis, On the Boussinesq approximation for a compressible fluid, Astrophys. J. **131**, 442 (1960).
[12] E. A. Spiegel, Convective instability in a compressible atmosphere. I, Astrophys. J. **141**, 1068 (1965).
[13] Y. Ricard, T. Alboussière, S. Labrosse, J. Curbelo, and F. Dubuffet, Fully compressible convection for planetary mantles, Geophys. J. Int. **230**, 932 (2022).
[14] E. Graham, Numerical simulation of two-dimensional compressible convection, J. Fluid Mech. **70**, 689 (1975).
[15] F. Cattaneo, N. H. Brummell, J. Toomre, A. Malagoli, and N. E. Hurlburt, Turbulent compressible convection, Astrophys. J. **370**, 282 (1991).
[16] J. Verhoeven, T. Wiesehöfer, and S. Stellmach, Anelastic versus fully compressible turbulent Rayleigh–Bénard convection, Astrophys. J. **805**, 62 (2015).
[17] J. J. Niemela, L. Skrbek, K. R. Sreenivasan, and R. J. Donnelly, Turbulent convection at very high Rayleigh numbers, Nature (London) **404**, 837 (2000).
[18] K.-Q. Xia, S. Lam, and S.-Q. Zhou, Heat-flux measurement in high-Prandtl-number turbulent Rayleigh-Bénard convection, Phys. Rev. Lett. **88**, 064501 (2002).
[19] S. Lam, X.-D. Shang, S.-Q. Zhou, and K.-Q. Xia, Prandtl number dependence of the viscous boundary layer and the Reynolds numbers in Rayleigh-Bénard convection, Phys. Rev. E **65**, 066306 (2002).
[20] R. Verzicco and R. Camussi, Numerical experiments on strongly turbulent thermal convection in a slender cylindrical cell, J. Fluid Mech. **477**, 19 (2003).
[21] J. J. Niemela and K. R. Sreenivasan, Confined turbulent convection, J. Fluid Mech. **481**, 355 (2003).
[22] M. Breuer, S. Wessling, J. Schmalzl, and U. Hansen, Effect of inertia in Rayleigh-Bénard convection, Phys. Rev. E **69**, 026302 (2004).
[23] S. Bhattacharya, M. K. Verma, and R. Samtaney, Prandtl number dependence of the small-scale properties in turbulent Rayleigh-Bénard convection, Phys. Rev. Fluids **6**, 063501 (2021).
[24] B. Castaing, G. Gunaratne, L. P. Kadanoff, A. Libchaber, and F. Heslot, Scaling of hard thermal turbulence in Rayleigh-Bénard convection, J. Fluid Mech. **204**, 1 (1989).
[25] O. Shishkina and C. Wagner, Analysis of sheet-like thermal plumes in turbulent Rayleigh–Bénard convection, J. Fluid Mech. **599**, 383 (2008).
[26] G. Silano, K. R. Sreenivasan, and R. Verzicco, Numerical simulations of Rayleigh–Bénard convection for Prandtl numbers between 10^{-1} and 10^4 and Rayleigh numbers between 10^5 and 10^9, J. Fluid Mech. **662**, 409 (2010).
[27] J. D. Scheel and J. Schumacher, Global and local statistics in turbulent convection at low Prandtl numbers, J. Fluid Mech. **802**, 147 (2016).
[28] Y. Zhang and Q. Zhou, Low-Prandtl-number effects on global and local statistics in two-dimensional Rayleigh–Bénard convection, Phys. Fluids **36**, 1 (2024).
[29] X. Chavanne, F. Chillà, B. Chabaud, B. Castaing, and B. Hebral, Turbulent Rayleigh-Bénard convection in gaseous and liquid He, Phys. Fluids **13**, 1300 (2001).
[30] X. He, D. Funfschilling, H. Nobach, E. Bodenschatz, and G. Ahlers, Transition to the ultimate state of turbulent Rayleigh-Bénard convection, Phys. Rev. Lett. **108**, 024502 (2012).
[31] K. P. Iyer, J. D. Scheel, J. Schumacher, and K. R. Sreenivasan, Classical 1/3 scaling of convection holds up to $\mathrm{Ra} = 10^{15}$, Proc. Natl. Acad. Sci. **117**, 7594 (2020).
[32] R. Samuel, R. Samtaney, and M. K. Verma, Large-eddy simulation of Rayleigh–Bénard convection at extreme Rayleigh numbers, Phys. Fluids **34**, 075133 (2022).
[33] D. Lohse and O. Shishkina, Ultimate Rayleigh-Bénard turbulence, Rev. Mod. Phys. **96**, 035001 (2024).
[34] S. Grossmann and D. Lohse, Scaling in thermal convection: A unifying theory, J. Fluid Mech. **407**, 27 (2000).
[35] S. Grossmann and D. Lohse, Thermal convection for large Prandtl numbers, Phys. Rev. Lett. **86**, 3316 (2001).
[36] G. Ahlers and X. Xu, Prandtl-number dependence of heat transport in turbulent Rayleigh-Bénard convection, Phys. Rev. Lett. **86**, 3320 (2001).

[37] P.-E. Roche, B. Castaing, B. Chabaud, and B. Hebral, Prandtl and Rayleigh numbers dependences in Rayleigh-Bénard convection, Europhys. Lett. **58**, 693 (2002).
[38] S. Bhattacharya, M. K. Verma, and R. Samtaney, Revisiting Reynolds and Nusselt numbers in turbulent thermal convection, Phys. Fluids **33**, 015113 (2021).
[39] A. Nikolaenko, E. Brown, D. Funfschilling, and G. Ahlers, Heat transport by turbulent Rayleigh-Bénard convection in cylindrical cells with aspect ratio one and less, J. Fluid Mech. **523**, 251 (2005).
[40] A. Pandey and M. K. Verma, Scaling of large-scale quantities in Rayleigh-Bénard convection, Phys. Fluids **28**, 095105 (2016).
[41] E. Brown, D. Funfschilling, and G. Ahlers, Anomalous Reynolds-number scaling in turbulent Rayleigh–Bénard convection, J. Stat. Mech. Theor. Exp. (2007) P10005.
[42] A. Pandey, A. Kumar, A. G. Chatterjee, and M. K. Verma, Dynamics of large-scale quantities in Rayleigh-Bénard convection, Phys. Rev. E **94**, 053106 (2016).
[43] O. Shishkina, M. S. Emran, S. Grossmann, and D. Lohse, Scaling relations in large-Prandtl-number natural thermal convection, Phys. Rev. Fluids **2**, 103502 (2017).
[44] G. T. Jarvis and D. P. Mckenzie, Convection in a compressible fluid with infinite Prandtl number, J. Fluid Mech. **96**, 515 (1980).
[45] S. Balachandar, D. A. Yuen, and D. Reuteler, Viscous and adiabatic heating effects in three-dimensional compressible convection at infinite Prandtl number, Phys. Fluids A: Fluid Dynamics **5**, 2938 (1993).
[46] D. Bercovici, G. Schubert, and G. A. Glatzmaier, Three-dimensional convection of an infinite-Prandtl-number compressible fluid in a basally heated spherical shell, J. Fluid Mech. **239**, 683 (1992).
[47] J. Toomre, N. Brummell, F. Cattaneo, and N. E. Hurlburt, Three-dimensional compressible convection at low Prandtl numbers, Comput. Phys. Commun. **59**, 105 (1990).
[48] H. P. Singh and K. L. Chan, A study of the three-dimensional turbulent compressible convection in a deep atmosphere at various Prandtl numbers, Astron. Astrophys. **279**, 107 (1993).
[49] P. J. Käpylä, Prandtl number dependence of stellar convection: Flow statistics and convective energy transport, Astron. Astrophys. **655**, A78 (2021).
[50] M. Manga and D. Weeraratne, Experimental study of non-Boussinesq Rayleigh–Bénard convection at high Rayleigh and Prandtl numbers, Phys. Fluids **11**, 2969 (1999).
[51] E. H. Anders and B. P. Brown, Convective heat transport in stratified atmospheres at low and high Mach number, Phys. Rev. Fluids **2**, 083501 (2017).
[52] J. P. John and J. Schumacher, Strongly superadiabatic and stratified limits of compressible convection, Phys. Rev. Fluids **8**, 103505 (2023).
[53] H. Tiwari, L. Sharma, and M. K. Verma, Compressible turbulent convection at very high Rayleigh numbers, Int. J. Heat Mass Transf. **242**, 126821 (2025).
[54] C. Ouyang, S. He, Q. Xu, Y. Luo, and W. Zhang, A MacCormack-TVD finite difference method to simulate the mass flow in mountainous terrain with variable computational domain, Comput. Geosci. **52**, 1 (2013).
[55] D. Liang, B. Lin, and R. A. Falconer, Simulation of rapidly varying flow using an efficient TVD-MacCormack scheme, Int. J. Numer. Methods Fluids **53**, 811 (2007).
[56] H. C. Yee, *Upwind and Symmetric Shock-Capturing Schemes* (National Aeronautics and Space Administration, Ames Research Center, Ames, IA, 1987).
[57] J. P. John and J. Schumacher, Compressible turbulent convection in highly stratified adiabatic background, J. Fluid Mech. **972**, R4 (2023).
[58] E. P. van der Poel, R. Ostilla-Mónico, R. Verzicco, and D. Lohse, Effect of velocity boundary conditions on the heat transfer and flow topology in two-dimensional Rayleigh-Bénard convection, Phys. Rev. E **90**, 013017 (2014).
[59] W. V. R. Malkus, The heat transport and spectrum of thermal turbulence, Proc. R. Soc. London A **225**, 196 (1954).
[60] R. H. Kraichnan, Turbulent thermal convection at arbitrary Prandtl number, Phys. Fluids **5**, 1374 (1962).
[61] B. I. Shraiman and E. D. Siggia, Heat transport in high-Rayleigh-number convection, Phys. Rev. A **42**, 3650 (1990).

[62] S. Grossmann and D. Lohse, Prandtl and Rayleigh number dependence of the Reynolds number in turbulent thermal convection, Phys. Rev. E **66**, 016305 (2002).
[63] J. Schmalzl, M. Breuer, and U. Hansen, On the validity of two-dimensional numerical approaches to time-dependent thermal convection, Europhys. Lett. **67**, 390 (2004).
[64] E. P. van der Poel, R. J. A. M. Stevens, and D. Lohse, Comparison between two- and three-dimensional Rayleigh–Bénard convection, J. Fluid Mech. **736**, 177 (2013).
[65] R. J. A. M. Stevens, D. Lohse, and R. Verzicco, Prandtl and Rayleigh number dependence of heat transport in high Rayleigh number thermal convection, J. Fluid Mech. **688**, 31 (2011).
[66] X.-M. Li, J.-D. He, Y. Tian, P. Hao, and S.-D. Huang, Effects of Prandtl number in quasi-two-dimensional Rayleigh–Bénard convection, J. Fluid Mech. **915**, A60 (2021).
[67] Wesseling, *Principles of Computational Fluid Dynamics*, 1st ed. (Springer-Verlag, Berlin, Heidelberg, 2000).
[68] R. H. Kraichnan, Inertial ranges in two-dimensional turbulence, Phys. Fluids **10**, 1417 (1967).
[69] R. Samuel and M. K. Verma, Bolgiano-Obukhov scaling in two-dimensional Rayleigh-Bénard convection at extreme Rayleigh numbers, Phys. Rev. Fluids **9**, 023502 (2024).
[70] A. Pandey and K. R. Sreenivasan, Transient and steady convection in two dimensions, J. Fluid Mech. **1015**, A42 (2025).
[71] U. Frisch, *Turbulence: The Legacy of A. N. Kolmogorov* (Cambridge University Press, Cambridge, UK, 1995).
[72] A. Tilgner, High-Rayleigh-number convection in spherical shells, Phys. Rev. E **53**, 4847 (1996).
[73] R. M. Kerr and J. R. Herring, Prandtl number dependence of Nusselt number in direct numerical simulations, J. Fluid Mech. **419**, 325 (2000).
[74] H. Tiwari, L. Sharma, and M. K. Verma, On the absence of the ultimate regime in turbulent thermal convection, Proc. Natl. Acad. Sci. USA **122**, e2513474122 (2025).
[75] S. Bhattacharya, R. Samtaney, and M. K. Verma, Scaling and spatial intermittency of thermal dissipation in turbulent convection, Phys. Fluids **31**, 075104 (2019).
[76] L. Sharma, M. Pathak, H. Tiwari, and M. K. Verma, Dataset for "Prandtl number dependence in turbulent compressible convection", Zenodo (2025), doi:10.5281/zenodo.17475388.